NUMERICAL INVESTIGATION ON THE IMPINGEMENT OF A CIRCULAR JET OF NANOFLUIDS ON A CIRCULAR FLAT PLATE

by

Dhimitri Kucuqi
Bachelor of Engineering, 2016
Mechanical Engineering
Ryerson University

A project
presented to Ryerson University

in partial fulfillment of the
requirements for the degree of

Master of Engineering
in the Program of
Mechanical and Industrial Engineering

Toronto, Ontario, Canada, 2018

Author’s Declaration

Author’s Declaration for Electronic Submission of a Project

I hereby declare that I, Dhimitri Kucuqi, am the sole author of this project. This is a true copy of the project, including any required final revisions.

I authorize Ryerson University to lend this project to other institutions or individuals for the purpose of scholarly research.

I further authorize Ryerson University to reproduce this project by photocopying or by other means, in total or in part, at the request of other institutions or individuals for the purpose of scholarly research.

I understand that my project may be made electronically available to the public.

Abstract

Numerical Investigation on the Impingement of a Circular Jet of Nanofluids on a Circular Flat Plate

Dhimitri Kucuqi

Master of Engineering

Mechanical and Industrial Engineering

Ryerson University, 2018

A numerical study was conducted to investigate and validate experimental convective heat transfer coefficient data associated with an Al_2O_3-H_2O nanofluid through the use of an impingement jet on a flat, circular disk. It was observed that, in conjunction with experimental data, nanofluids provided increased local convective heat transfer coefficients in comparison to the base fluid. Nanofluid concentrations outlined in the experimental model, from 0.0198 to 0.0757 wt%, were investigated in a numerical model and resulting convective heat transfer coefficients were compared. In contrast to the experimental model, the maximum heat transfer enhancement occurred at the nanofluid concentration of 0.0757 wt%. In addition, several other models were tested with various Reynolds numbers and jet height-to-jet diameter ratios for further investigation along with discussion of sources of error. Overall, in comparison to experimental data, the lowest percentage errors achieved for the Reynolds numbers of 4245.7 and 8282 were 17.9% and 34.9%, respectively.

Acknowledgements

I would like to express my gratitude to my supervisor, Dr. Tooraj Yousefi, for his guidance and support throughout the course of this project.

I would also like to thank Dr. Bassam Jubran, who provided a wealth of knowledge and information in understanding the core concepts of this project.

Lastly, I would also like to express my gratitude to my family and friends, for their encouragement and support in completing this project.

Table of Contents

Abstract iii

List of Tables vii

List of Figures viii

Nomenclature x

1.0 Introduction 1

1.1 Problem Statement and Importance 1

1.2 Goals and Objectives 2

1.3 Geometry Design 2

2.0 Literature Review 4

2.1 Introduction to Jet Impingement 4

2.2 Singular Jet Impingement Flow Characteristics and Structure 5

2.2.1 Primary Regions and Subregions 5

2.2.2 Transition Region 8

2.2.3 Turbulence Development and Vortex Generation 9

2.3 Singular Jet Impingement Heat Transfer Characteristics and Governing Equations 11

2.3.1 Effect of Jet Height-to-Jet Diameter (H/D) ratio on the Heat Transfer Distribution 12

2.4 Heat Transfer Enhancement 14

2.4.1 Introduction to Nanofluids 14

2.4.2 Preparation of Nanofluids 15

2.4.3 Correlations of Properties of Nanofluids 16

2.4.4 Limitations 17

2.5 “Experimental investigation on heat transfer enhancement due to Al_2O_3 – water nanofluid using impingement of round jet on circular disk” by B. Jaberi, T. Yousefi, B. Farahbakhsh, M.Z. Saghir [2] 18

3.0 Preliminary Processing and Description of Activities 19
3.1 Assumptions and Simplifications 19
3.2 Meshing Considerations and Sensitivity Study 20
3.3 Modeling Parameters, Properties, and Boundary Conditions 25
4.0 Numerical Simulation Results and Validation 29
4.1 Turbulence Model Optimization and Selection 29
4.2 Analysis of the Local Heat Transfer Coefficient Variation with Radial Distance for Reynolds Numbers of 4245.7 and 8282 34
4.3 Analysis of the Average Heat Transfer Coefficient Variation for Reynolds Numbers of 4245.7 and 8282 39
4.4 Analysis of the Velocity and Pressure Profiles 41
5.0 Additional Analysis 45
5.1 Analysis of the Average Heat Transfer Coefficient for Various Reynolds Numbers and H/d Ratios 45
5.2 Analysis of the Stagnation Heat Transfer Coefficient for Various Reynolds Numbers and H/d Ratios 47
5.3 Analysis of the Average Heat Transfer Coefficient for Various Nanofluid Concentration, Reynolds Numbers, and H/d Ratios 48
5.4 Analysis of the Variation of Local Heat Transfer Coefficient vs. Radial Distance for Various Reynolds Numbers and H/d Ratios 50
6.0 Error Analysis 55
7.0 Future Work 57
8.0 Review and Conclusions 58
References 59

List of Tables

Table 1.3.1 – Design Parameters [2] 3
Table 3.2.1 – Mesh Sensitivity (Grid Independence) Study Summary 21
Table 3.2.2 – Mesh Parameters 22
Table 3.2.3 – Surface Inflation Mesh Parameters 23
Table 3.3.1 – Fluid (Water) Properties [2] 25
Table 3.3.2 – Surface (Aluminum) Properties [2] 25
Table 3.3.3 – Nanoparticle (Al_2O_3) Properties [2] 25
Table 3.3.4 – Nanofluid (Al_2O_3-Water) Properties [2] 27
Table 3.3.5 – Summary of Boundary Conditions [2] 27
Table 4.1.1 – Experimental Data [2] 32
Table 4.1.2 – Turbulence Model Optimization for H_2O as the Working Fluid at Re = 4245.7 ... 32
Table 4.1.3 – Turbulence Model Optimization for H_2O as the Working Fluid at Re = 4245.7 (C.) 33
Table 4.1.4 – Average and Maximum Percentage Errors for H_2O as the Working Fluid 33
Table 4.2.1 – Experimental Data for Re = 4245.7 36
Table 4.2.2 – Experimental Data for Re = 8282 36
Table 4.2.3 – Percentage Errors for Re = 4245.7 37
Table 4.2.4 – Percentage Errors for Re = 8282 37

List of Figures

Figure 1.3.1 – 2D Jet Impingement Model Geometry and Features 3
Figure 2.2.1.1 – Impinging Jet Flow Regions and Structure [3] 5
Figure 2.2.1.2 – Detailed Impinging Jet Flow Regions and Structure [6] 6
Figure 2.2.1.3 – Free Jet Region Flow Structure [3] 6
Figure 2.2.2.1 – Laminar to Turbulent Transition [6] 8
Figure 2.2.3.1 – Vortex Generation [3] 10
Figure 2.2.3.2 – Overall Vortex Geometry [3] 11
Figure 2.3.1.1 – Stagnation Point Heat Transfer Coefficient [10] 13
Figure 3.2.1 – Mesh Sensitivity Analysis 21
Figure 3.2.2 – 2D Model Meshing 24
Figure 3.2.3 – Surface Boundary Layer Mesh Resolution 24
Figure 4.1.1 – Turbulence Model Optimization for H_2O as the Working Fluid 30
Figure 4.1.2 – Lowest Percentage Error Turbulence Models 31
Figure 4.2.1 – Local Heat Transfer Coefficient for Re = 4245.7 35
Figure 4.2.2 – Local Heat Transfer Coefficient for Re = 8282 35
Figure 4.2.3 - Percentage Errors for Re = 4245.7 38
Figure 4.2.4 - Percentage Errors for Re = 8282 38
Figure 4.3.1 – Average Heat Transfer Coefficient for Various Reynolds Numbers 40
Figure 4.4.1 – Velocity Profile for Re = 4245.7 41
Figure 4.4.2 – Stagnation Region Velocity Profile for Re = 4245.7 42
Figure 4.4.3 – Velocity Profile for Re = 8282 42
Figure 4.4.4 – Stagnation Region Velocity Profile for Re = 8282 43
Figure 4.4.5 – Pressure Profile for Re = 4245.7 43
Figure 4.4.6 – Pressure Profile for Re = 8282 44
Figure 5.1.1 – Average Heat Transfer Coefficient for H_2O at Various Reynolds Numbers and H/d Ratios 46
Figure 5.1.2 – Average Heat Transfer Coefficient for 0.0757 wt% Nanofluid at Various Reynolds Numbers and H/d Ratios 46
Figure 5.2.1 – H_2O Stagnation Heat Transfer Coefficient 47

Figure 5.2.2 – 0.0757 wt% Nanofluid Stagnation Heat Transfer Coefficient 48
Figure 5.3.1 – Variation of Nanofluid Concentration with Reynolds Number and H/d = 2 49
Figure 5.3.2 – Variation of Nanofluid Concentration with Reynolds Number and H/d = 5.11 ... 49
Figure 5.3.3 – Variation of Nanofluid Concentration with Reynolds Number and H/d = 10 50
Figure 5.4.1 – Local Heat Transfer Coefficient vs. Radial Distance for H_2O at H/d = 2 51
Figure 5.4.2 – Local Heat Transfer Coefficient vs. Radial Distance for 0.0757 wt% at H/d = 2. 52
Figure 5.4.3 – Local Heat Transfer Coefficient vs. Radial Distance for H_2O at H/d = 5.11 52
Figure 5.4.4 – Local Heat Transfer Coefficient vs. Radial Distance for 0.0757 wt% at H/d = 5.11 53
Figure 5.4.5 – Local Heat Transfer Coefficient vs. Radial Distance for H_2O at H/d = 10 53
Figure 5.4.6 – Local Heat Transfer Coefficient vs. Radial Distance for 0.0757 wt% at H/d = 1054

Nomenclature

c_p	specific heat capacity (J/kgK)
d	nozzle diameter (m)
de	nanoparticle diameter (m)
H	jet height (m)
h	heat transfer coefficient, (W/m^2K)
L	nozzle length (m)
k	thermal conductivity (W/mK)
Nu	nusselt number (-)
N_1	numerical value 1
N_2	numerical value 2
q	heat flux (w/m^2)
Re	reynolds number (-)
r	radial position (m)
Δs	first layer thickness (m)
T	temperature (K)
u, U	velocity (m/s)
V	volume (m^3)
w	weight (kg)

Greek Symbols

α	thermal diffusivity (m^2/s)
μ	dynamic viscosity (Pa s)
ρ	density (kg/m^3)
φ	volume fraction (%)

Subscripts

f	fluid
bf	base fluid

nf	nanofluid
np	nanoparticle
r	nanofluid-to-base fluid ratio
e, ∞	free stream
s, as	disc surface, adiabatic surface
ref	reference (bulk)
solute	refers to nanoparticle
solvent	refers to water

1.0 Introduction

1.1 Problem Statement and Importance

In the past several decades, the need for highly efficient and extremely compact electronic components has increased substantially. In turn, this advanced development has highlighted the importance of efficient cooling in order to maintain the capabilities of electronic components, such as the Central Processing Unit (CPU). Current conventional methods (but still applicable in certain conditions) employ the use of heat sinks, heat pipes, fins, fan arrays, liquid cooling (more recent), etc. as primary cooling methods, which have generally provided the necessary cooling for optimal electronic component performance and prevention of extreme thermal stresses from occurring due to prolonged use at high component temperatures [1]. However, several factors, primarily strict design constraints and heat dissipation requirements, limit the applicability of the aforementioned cooling methods, which ultimately translates to the need for smaller and more powerful electronic components.

Current technological advancements in the field of thermal cooling systems have provided promising results in overcoming several limiting factors. In particular, jet impingement cooling has been extensively examined as a cooling system for electronic components due to its ability to fit within design requirements and still provide high cooling potential [1]. In addition, fluids utilized for impingement cooling can vary, which allows for optimal selection and heat transfer capabilities along with flexibility for different applications. More recently, nanoparticles suspended within a base fluid, such as water, have shown to provide enhanced characteristics and properties as an overall fluid and ultimately, provide higher heat transfer coefficients [2]. These topics will be discussed in detail in a subsequent section.

1.2 Goals and Objectives

The purpose of this report was to numerically investigate and validate an experimental analysis by B. Jaberi et al. [2] associated with the impingement of a circular jet of nanofluids on a circular flat plate. The numerical study involves analyzing and validating the effect of nanoparticle concentration with respect to the experimental study, along with analyzing the effect of various Reynolds numbers, jet height-to-jet diameter ratios, and other factors to simulate and optimize the capabilities for nanofluid jet impingement. The numerical study consists of the following sections and/or chapters:

i) research of analytical, experimental, and numerical scholarly papers regarding jet impingement cooling for various applications,
ii) collection of significant data, such as variables, initial conditions, etc., required for modeling,
iii) modeling of the jet impingement cooling scenario using ANSYS Fluent,
iv) analysis of results and validation with chosen model,
v) discussion of discrepancies or errors associated with modeling, and
vi) conclusions and recommendations for future development.

1.3 Geometry Design

From the experimental study, several parameters, such as nozzle diameter, surface diameter, jet height, etc. were obtained and utilized to develop the initial model for the jet impingement scenario. The jet impingement scenario was designed as a 2D model given its axisymmetric characteristics that produce accurate results while keeping computational costs relatively low. Figure 1.3.1 depicts the finished geometry as the 2D model, with selected edges of the model were utilized as the inlet, outlets, surfaces, etc., that incorporate the nozzle and fluid region while Table 1.3.1 outlines the various parameters used to develop the 2D model.

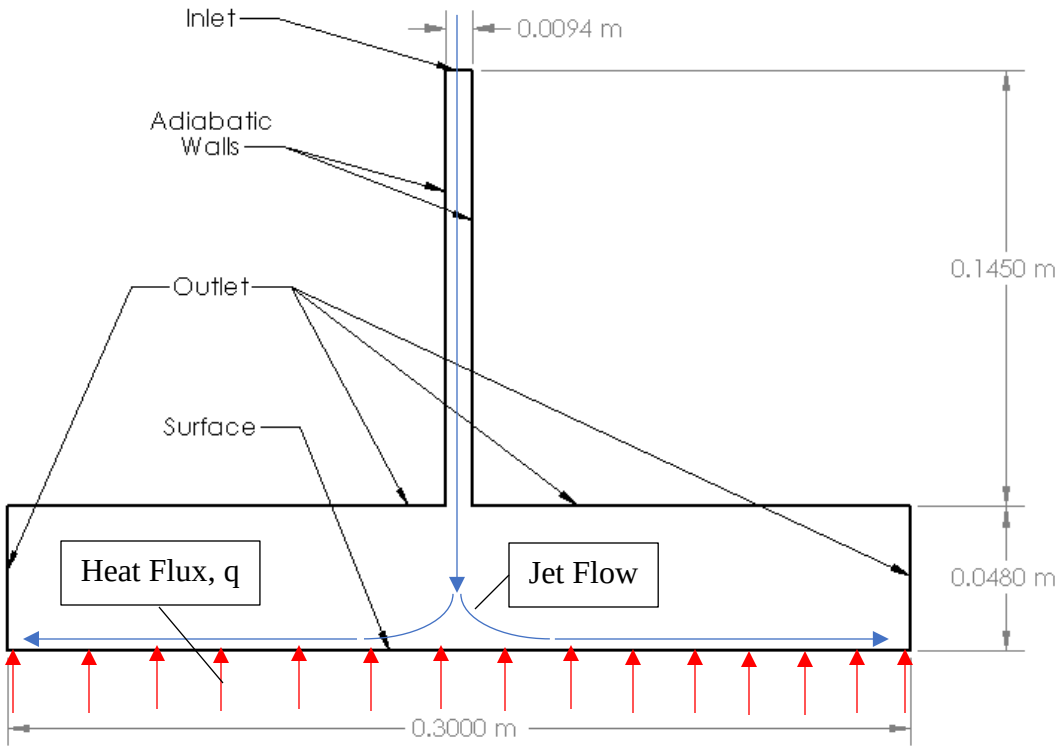

Figure 1.3.1 – 2D Jet Impingement Model Geometry and Features

The outlined edges involve the inlet for the fluid, the adiabatic walls that guide the fluid to the surface ensuring no heat loss, the outlet where the fluid is allowed to flow to surroundings, and the surface that simulates the heat aluminum disk surface.

Table 1.3.1 – Design Parameters [2]

Parameter	**Value**
Nozzle Inlet Diameter, d	0.0094 m
Nozzle Inlet Length, L	0.1450 m
Jet Height, H	0.0480 m
Surface Diameter, D	0.3000 m

2.0 Literature Review

2.1 Introduction to Jet Impingement

As outlined briefly in the introduction section, jet impingement can be utilized as a form of cooling that provides a directed jet of fluid towards a specific surface for either transferring or removing thermal energy [3,4]. In the past decade, several applications have been developed primarily for cooling purposes, which include electronic equipment cooling, gas turbine cooling, material/steel/glass processing, etc. [4]. Due to the ever-increasing design constraints for electronic components, jet impingement has been previously examined and labeled as a potential improvement or replacement to current conventional methods that utilize heat sinks and other features.

Various scenarios have been created that utilize numerous impinging jets that form a structured array to maximize cooling in order to avoid or prevent any abnormal thermal stresses from prolonged use at high temperatures [1]. One example is Central Processing Unit (CPU) overclocking. CPU overclocking results in higher-than-normal heat loads which, for conventional cooling methods, cannot be easily removed due to cooling constraints. As a result, prolonged or extended use at overclocked temperatures greatly reduces the performance and life expectancy of the component. Another example is gas turbine cooling, which utilizes a fraction of the air from the compressor to provide cooling through jet impingement to turbine vanes, which would otherwise result in catastrophic damage to the turbine system [5]. Overall, the application of jet impingement cooling has shown to provide considerable improvement in the efficiency, power, and lifespan of various applications, particularly electronics [5]. However, due to its nature, Zuckerman & Lior [3] have described that although jet impingement cooling provides higher heat transfer coefficients than other methods, it can result in a highly non-uniform temperature distribution on the surface. This can adversely affect the integrity of the electronic component [3,5].

2.2 Singular Jet Impingement Flow Characteristics and Structure

2.2.1 Primary Regions and Subregions

Depending on the application and orientation of the jet, various flow characteristics can be described. However, majority of applications involve a relatively flat and level surface with a perpendicularly oriented impinging jet, which is the primary structure that will be analyzed in this study.

The physical flow structure present within a single impinging jet involves several regions and subregions that define important heat and mass transfer characteristics. Figures 2.2.1.1 and 2.2.1.2 depict the three primary regions within an impinging jet are the i) free jet region, ii) stagnation flow region, and iii) wall jet region. Figure 2.2.1.3 outlines the velocity profile at different stages following the nozzle exit with the aforementioned regions.

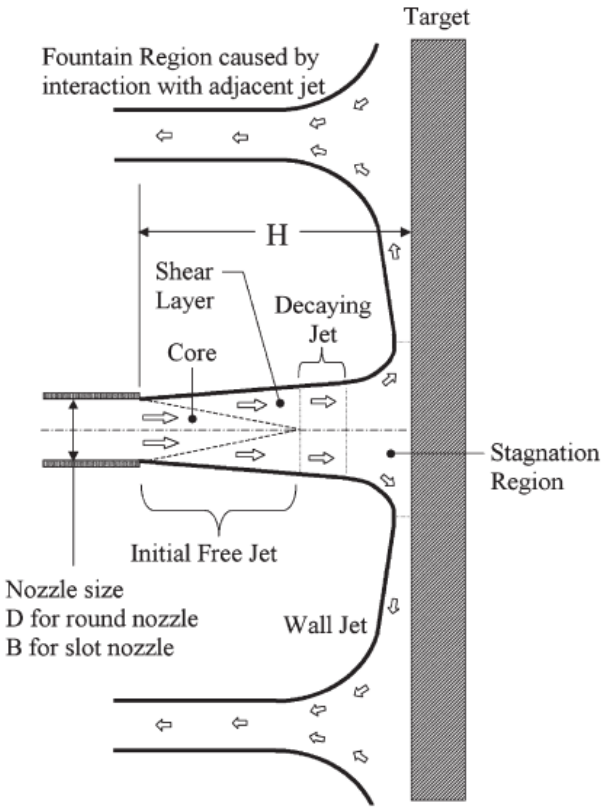

Figure 2.2.1.1 – Impinging Jet Flow Regions and Structure [3]

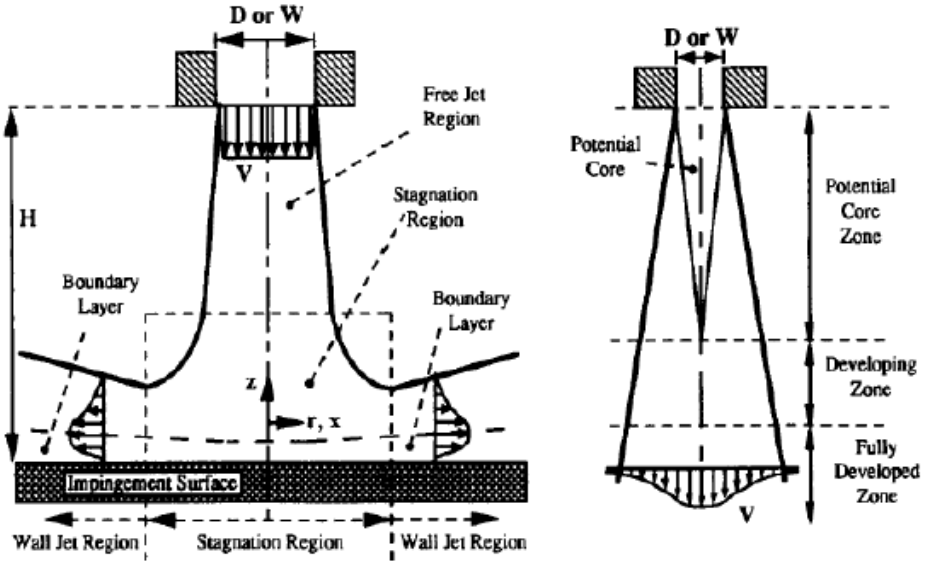

Figure 2.2.1.2 – Detailed Impinging Jet Flow Regions and Structure [6]

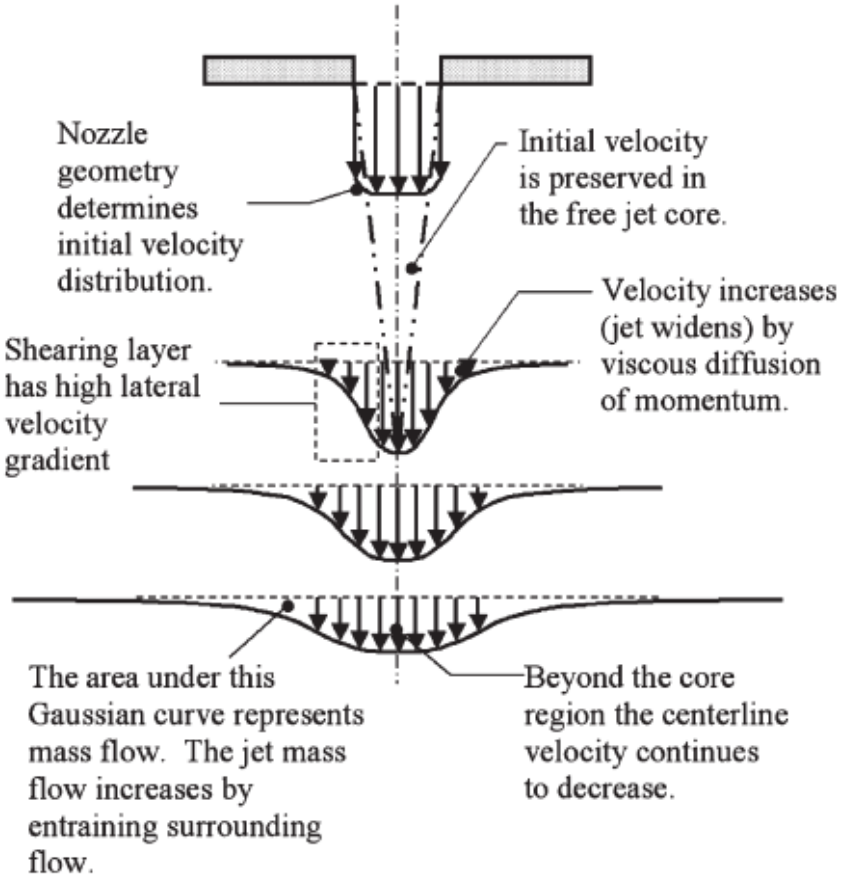

Figure 2.2.1.3 – Free Jet Region Flow Structure [3]

In Figures 2.2.1.1 and 2.2.1.2, the free jet region is the primary region that involves the transfer of mass, momentum, and energy of the fluid to the surface, where it decays in profile and speed due to expansion of the fluid to fill the surroundings. As outlined by Zuckerman & Lior [3], the distance from the nozzle exit to the surface influences the free jet region immensely. Small distances, such as a distance of 2 diameters, prevent the free jet region from fully forming [3]. In cases where this distance is substantial enough to support the free jet region, there are three subregions within the free jet region, which are the i) potential core zone, ii) developing core zone, and iii) fully developed zone, as shown in Figure 2.2.1.2. The potential core is the primary subregion immediately following the nozzle exit, where the velocity profile is nearly identical to the exit velocity and dissipates with increasing distance [3,6]. The developing and fully developed zones are the secondary and tertiary subregions where the velocity profile initially starts to widen as it exits the nozzle and continually decreases in velocity with increasing distance from the potential core [3]. The trend shown in Figure 2.2.1.3 depicts the start of the Gaussian distribution that extends into the two following subregions [3].

The stagnation flow region is the secondary region, as shown in Figures 2.2.1.1 and 2.2.1.2, where the velocity of the fluid decreases to zero, while the pressure at the surface increases due to the buildup of the fluid [3]. The highest static pressures in the system can be expected to occur directly at the point of impingement, where increasing distance from this point radially outwards results in increasing local velocities and decreasing local pressures of the fluid [3]. The drastic variation in fluid direction results in a non-uniform flow pattern that produces various stresses which ultimately disturb local heat transfer rates due to the production of vortices and greater turbulence [3,6].

The wall jet region is the tertiary region as shown in Figures 2.2.1.1 and 2.2.1.2, where the fluid is directed radially outward and the boundary layer increases in thickness with increasing distance from the stagnation region [3]. Zuckerman & Lior [3] have outlined that the boundary layer at the surface "…has a typical thickness of no more than 1% of the jet diameter." Consequently, the fluid velocity decreases as the fluid moves further from the impinging jet but due to the conservation of momentum, can accelerate for a short period of time immediately after redirection of the fluid [3].

Further analysis dictates that multiple impinging jets have individual effects on one another, which require consideration in analyzing the heat transfer characteristics at points of interaction. Figure 2.2.1.1 depicts an additional fountain region that forms from the interaction between two neighboring impinging jets at the far wall jet regions. The interaction and combination of these two flows could potentially result in a single upward flow that could greatly affect local heat transfer rates in the immediate surface region. This phenomenon can result in the highly non-uniform temperature distribution, which can affect overall integrity of the component as previously mentioned [5].

2.2.2 Transition Region

In itself, the transition region within the wall jet region is extremely important to individually capture and analyze due to the heat transfer capabilities that can be obtained when the flow transitions from laminar to turbulent. As shown in Figure 2.2.2.1, the laminar to turbulent transition region/zone, which typically occurs at a distance of two nozzle diameters from point of impingement, has been predicted to increase heat transfer characteristics due to the formation of vortices within the turbulent boundary layer that improve fluid mixing and the ability for greater heat dissipation, as opposed to the laminar region that promotes very little to no fluid mixing [4]. This disturbance in the boundary layers near the wall results in a second peak and provides an enhancement in the Nusselt number and local heat transfer coefficients [4].

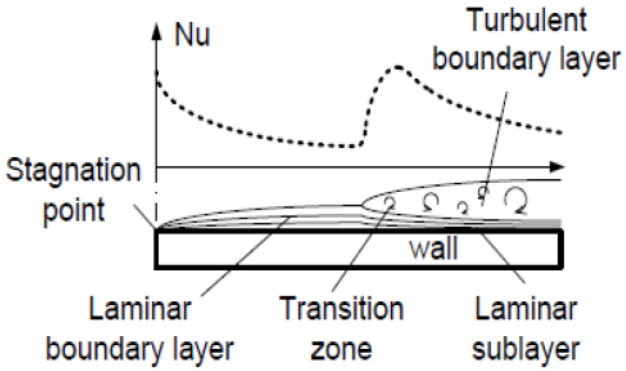

Figure 2.2.2.1 – Laminar to Turbulent Transition [6]

Several other factors, such as the Reynolds number (Re) and jet height-to-jet diameter (H/D) ratio, influence the physical structure of the transition region. On one hand, lower or higher Reynolds number affect the intensity of the jet flow, which proportionally provide lower or higher heat transfer coefficients, respectively. On the other hand, when the jet height-to-jet diameter ratio is increased or decreased, the corresponding arrival velocity at the point of impingement is inversely proportional and thus decreases and increases respectively [7]. In turn, the transition region and its effects on heat transfer characteristics are highly dependent on these relationships, as large jet height-to-jet diameter ratios (≥ 7) do not have significantly pronounced or drastic transition regions, while small jet height-to-jet diameter ratios (< 7) have noticeable transition regions as depicted with the second peak in the local Nusselt number distribution [4,7].

2.2.3 Turbulence Development and Vortex Generation

Jet and fluid behavior can be attributed to three particular ranges of Reynolds number for a circular jet. With a Reynolds number less than 1000, flow behavior depicts laminar, or slow, flow characteristics [3]. With a Reynolds number greater than 3000, flow behavior depicts turbulent characteristics [3]. In between this range of Reynolds numbers, 1000 and 3000, a transition region exists where the flow is not entirely laminar but not entirely turbulent. As previously mentioned, it is evident that turbulence has a significant impact on the overall heat and mass transfer characteristics, which is due to the mixing and diffusion of the fluid with other fluids and surface interactions [3].

Several characteristics of turbulent flow can be examined in detail, particularly vortex and eddy generation. Vortex generation can be attributed to the well-known Kelvin-Helmholtz instabilities, which occur typically when there is velocity shear present within a fluid, or when a difference in velocity is present at the boundary between two separate fluids (e.g. water and air) [7]. Due to the natural and physical characteristics of the fluid(s), these instabilities can produce large vortices that greatly increase the overall turbulence in the system. In turn, this affects several parameters of the fluid, including, but not limited to, the jet spread, potential core length, etc. [7].

As depicted by Zuckerman & Lior, Figures 2.2.3.1 and 2.2.3.2 are very indicative of the generation of vortices, with several detailed stages. The initial jet region depicts the start of the vortex ring due to the shearing of the fluid at the very edges of the jet. As the jet continues towards the surface, much larger vortex rings and eddies form to create greater instabilities in the system [3]. Combined with the increasing pressure around the stagnation region, these vortices and eddies are redirected along the surface, as shown in Figure 2.2.3.2 [3]. In addition, the turbulent jet flow along the wall can potentially promote "secondary vortices", which have local sections of flow separation [3]. Numerous studies have investigated and concluded this particular phenomenon the main cause of the second peak in heat transfer coefficients, while other studies have attributed it to the "…shear forces in the thin accelerating region immediately outside the stagnation region" [3].

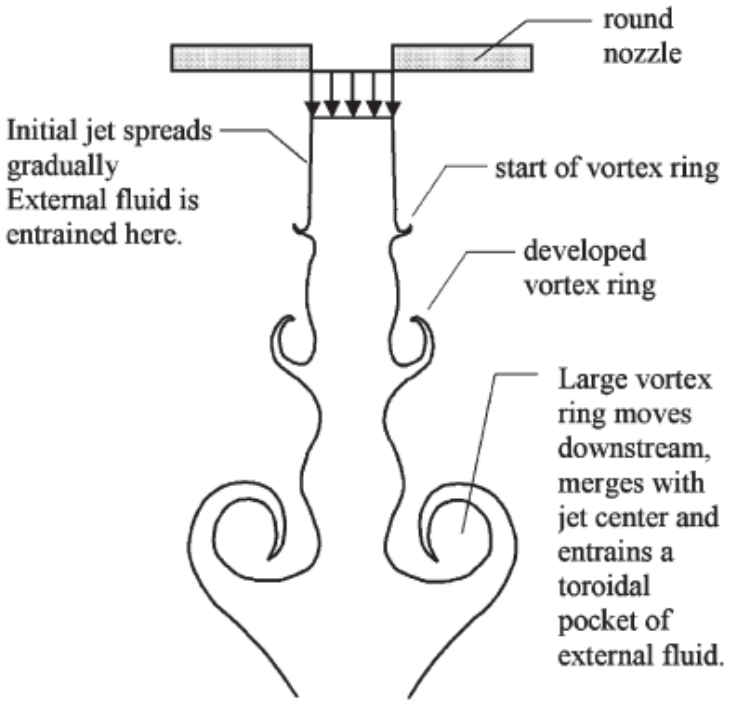

Figure 2.2.3.1 – Vortex Generation [3]

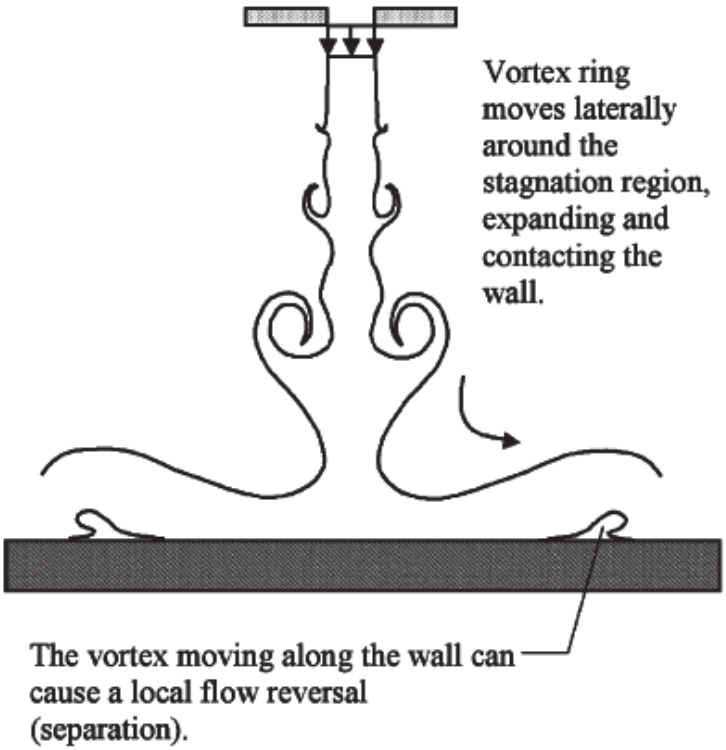

Figure 2.2.3.2 – Overall Vortex Geometry [3]

2.3 Singular Jet Impingement Heat Transfer Characteristics and Governing Equations

Several numerical and experimental studies completed by Chaudhari et. al [1], Anwarullah et al. [5], Jayaraman [6], Jensen & Walther [8], and other individuals have utilized numerous parameters and variables to provide an extensive analysis of the heat transfer characteristics related to jet impingement. The primary variables required for an in-depth analysis include the Nusselt number (Nu), Reynolds number (Re), heat transfer coefficient (h), jet height-to-jet diameter ratio/dimensionless height (H/d), and radial distance-to-jet diameter ratio/dimensionless radial distance (r/d).

As defined in “Heat Transfer” by Mills & Ganesan [9], the Nusselt and Reynolds numbers can be defined as,

$$Nu = \frac{hd}{k_f}; Re = \frac{\rho_f U_f d}{\mu_f}$$

Additionally, Newton's Law of Cooling for Convective Heat Transfer as defined in "Heat Transfer" by Mills & Ganesan [9] is defined as,

$$q_s = h\left[T_s(r) - T_{ref}(r)\right] \rightarrow h = \frac{q_s}{T_s(r) - T_{ref}(r)}$$

The recovery factor is also a significant parameter, which as defined in "Heat Transfer" by Mills & Ganesan [9] "…can be viewed as the fraction of kinetic energy of the free stream fluid, which is recovered as thermal energy in the fluid adjacent to an adiabatic wall,"

$$T_{as} = T_e + r\frac{u_e^2}{2c_{p,f}} \rightarrow r = \frac{2c_{p,f}(T_{as} - T_e)}{u_e^2}$$

In analyzing the heat transfer distribution associated with an impinging jet, several geometric and flow characteristics need to be considered as they have substantial effects on the overall jet performance. Determining optimal impinging jet characteristics involves examining primary regions of interest, which include the stagnation point, i.e. r/d = 0 or the direct center of impingement where velocity is assumed to be zero, and the transition region, where specific cases produce the second peak in the heat transfer distribution.

2.3.1 Effect of Jet Height-to-Jet Diameter (H/D) ratio on the Heat Transfer Distribution

One important geometric property of an impinging jet is the jet height-to-jet diameter ratio or dimensionless height (H/d). Several studies have been conducted to analyze the effect of the H/d ratio on the previously mentioned stagnation point and transition regions, which have provided substantial results regarding the heat transfer distribution for these particular regions.

Figure 2.3.1.1 depicts the stagnation point Nusselt number, Nu_O, against the dimensionless nozzle-to-plate spacing, or H/d ratio as studied by Gardon & Cobonpue in a study by the National Aeronautics Space Administration (NASA) [10]. It is evident that as the H/d ratio increases to approximately 6-8, Nu_O reaches a maximum, regardless of the nozzle diameter and Reynolds

number. As highlighted by O'Donovan [7], the increase in Nu_O from an H/d ratio of 0-6 has been attributed "…to the penetration of turbulence induced mixing from the shear layer to the centerline of the jet" [7]. Beyond an H/d ratio of 8, the distance between the plate and the nozzle exit has shown to be significantly large enough that a lower jet velocity impinges on the surface, which in turn, reduces the overall heat transfer capabilities of the jet and the effect is depicted in Figure 2.3.1.1 [7]. Other studies highlighted by O'Donovan [7] have shown to provide a maximum Nu_O at approximately 10% beyond the potential core length.

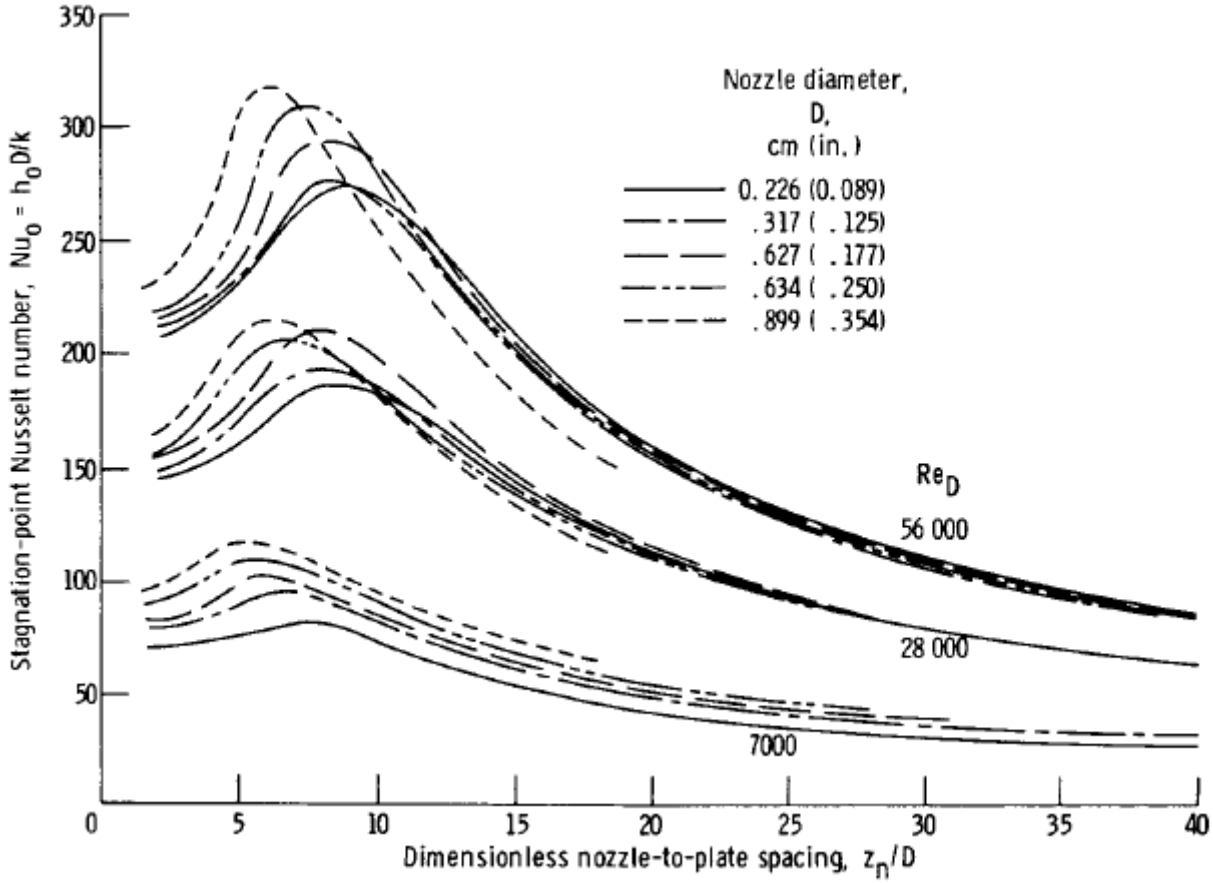

Figure 2.3.1.1 – Stagnation Point Heat Transfer Coefficient [10]

In addition to the stagnation point region, the transition region is also highly influenced by the H/d ratio, which in specific circumstances, provide the well-known second peak in the heat transfer distribution. As highlighted by Figure 2.2.2.1 previously, it is evident that the transition region produces greater mixing due to turbulent flow properties, which produces the second peak and enhances the heat transfer distribution around the immediate region. However, only H/d ratios less

than 5 typically establish the second peak in the Nusselt number distribution, which is consistent for Reynolds numbers up to 124,000, as defined by O'Donovan [7]. On one hand, in cases where H/d ratios are relatively small (≈2-3), the second peaks actually produce higher local Nusselt numbers than the stagnation region [7]. On the other hand, for large H/d ratios, the second peaks dissipate and the overall heat transfer distribution follows a decaying exponential curve.

2.4 Heat Transfer Enhancement

Several heat transfer enhancement methods have been investigated extensively, which include adjusting the geometric and fluid characteristics of the impinging jet. Adjusting the jet impingement angle, chamfered nozzle exits, jet excitation, and introduction of nanoparticles within a base fluid are a few of the ways that have been studied to improve the overall heat transfer of an impinging jet [3,7]. As per the scope of this report, the study of nanofluids will be the primary focus as an enhancement technique.

2.4.1 Introduction to Nanofluids

Nanoparticles, which include various metallic and non-metallic solids such as aluminum oxide (Al_2O_3), copper oxide (CuO), silica (SiO_2), and others, have the potential to improve the overall heat transfer due to an increase in the effective thermal conductivity when situated within a base fluid, such as water. Additionally, the promotion of turbulence from particle movement has demonstrated to increase the stagnation Nusselt number by a factor of up to 2.7 [3]. However, specific limitations are imposed on the weight/volume fraction of particles within the base fluid, as the effect of large volume fractions of particles could potentially damage or erode the impingement surface [3].

Moreover, as highlighted by Wu & Zhao [11], nanofluids produce improvements in overall heat transfer but have a nonlinear relationship between the amount or concentration of nanoparticles within a fluid and the effective thermal conductivity, which could limit its application and requires further investigation.

Typically, the mixture model along with mass and energy balances were utilized when analyzing solid-fluid mixtures, in order to provide overall effective thermal properties (e.g. density, thermal conductivity, specific heat capacity, viscosity, etc.) of the mixture [11]. However, due to the size of the nanoparticles, the predictive model for fluid properties is complicated, where certain nanoparticles have proportional increases in thermal conductivity based on their volume fraction and surface area [11]. Many experimental observations have outlined that Brownian motion, which is the random motion or movement of particles within a fluid that results from interaction with smaller molecules of the fluid, plays an important role in enhancing fluid properties [11]. As highlighted by B. Jaberi et al. [2], several studies have been done to investigate the heat transfer mechanisms that occur between submerged nanoparticles and the surrounding fluid, in which many have proved that Brownian motion does contribute to the effective thermal properties of nanofluids, particularly thermal conductivity.

From an analysis of experimental and numerical techniques, some generalized information of nanofluids have been proposed by Wu & Zhao [11], which outline that nanofluids i) require a balance between concentration, particle size, etc. to provide appropriate heat transfer enhancement, ii) act primarily as a single-phase, as opposed to multi-phase, fluids given that the aforementioned criteria has limits, and iii) do not simply provide heat transfer enhancement from an analysis of thermal conductivity alone [11]. Further analysis regarding Brownian motion and other assumptions will need to be confirmed through testing and experimentation.

2.4.2 Preparation of Nanofluids

Nanofluid preparation is complex in that in order to establish an equilibrium between the base fluid and the nanoparticles, special preparation is necessary to avoid any large buildup in specific zones of the mixture [12]. This large buildup of particles, also known as agglomeration, is a distinct issue in preparing any nanofluid. Two particular methods are extensively utilized in the preparation of nanofluids, which are the single-step and two-step methods [12]. The single-step method employs the use of physical/chemical reactions to produce nanofluids with a lower amount of agglomeration, but has the disadvantage of excess reactants remaining within the fluid due to not achieving 100% reaction [13]. As a result, this would affect the stability of the nanofluids and its

application. On the other hand, the two-step method employs the use of dried nanoparticles, which vary in structure and physical/chemical properties, and dispersing them into base fluids with the use of ultrasonic equipment for effective dispersal of nanoparticles [2,12,13]. However, as highlighted by B. Jaberi et al. [2], nanoparticles still agglomerate due to London-Van der Waal forces and thus, require additional techniques to control and reduce agglomeration, which include electro-static repulsion, controlling the pH of the mixture, and adding surface active agents [12,13].

2.4.3 Correlations of Properties of Nanofluids

Based on the experimental study by B. Jaberi et al., several equations and correlations were developed to approximate the nanofluid density, specific heat capacity, and the viscosity [2]:

$$\rho_{nf} = (1-\varphi)\rho_{bf} + \varphi\rho_{n\rho}$$

$$c_{p,nf} = \frac{(1-\varphi)\left(\rho c_p\right)_{bf} + \varphi\left(\rho c_p\right)_{np}}{\rho_{nf}}$$

$$\mu_{nf} = \mu_{bf}(1 + 2.5\varphi)$$

Other correlations were determined experimentally in a study by K.V. Sharma et al. [15] for heat transfer coefficients for various nanofluid including Al_2O_3 in water. However, as mentioned previously, K.V. Sharma et al. [15] outlines that the various techniques have an impact on the overall thermal conductivity and stability of the mixture. Similar to the equations outlined above, density and specific heat capacity can be outlined as follows [15]:

$$\rho_{nf} = \left(1 - \frac{\phi}{100}\right)\rho_{bf} + \left(\frac{\varphi}{100}\right)\rho_{np}$$

$$c_{p,nf} = \frac{\frac{\varphi}{100}\left(\rho c_p\right)_{np} + \left(1 - \frac{\varphi}{100}\right)\left(\rho c_p\right)_{bf}}{\rho_{nf}}$$

For the thermal conductivity and absolute viscosity, empirical relationships and regression equations were evaluated and formulated to estimate values for various particle sizes above 20 nm and volume concentration less than 4.0% [15]. Numerous other studies from different authors and their data were utilized to develop the following relationships for thermal conductivity and absolute viscosity [15]:

$$k_r = \frac{k_{nf}}{k_{bf}} = \left[0.8938\left(1+\frac{\varphi}{100}\right)\left(1+\frac{T_{nf}}{70}\right)^{0.2777}\left(1+\frac{de_{np}}{150}\right)^{-0.0336}\left(\frac{\alpha_{np}}{\alpha_{bf}}\right)^{0.01737}\right]$$

$$\mu_r = \frac{\mu_{nf}}{\mu_{bf}} = C_1\left(1+\frac{\varphi}{100}\right)^{11.3}\left(1+\frac{T_{nf}}{70}\right)^{-0.038}\left(1+\frac{de_{np}}{170}\right)^{-0.061}$$

However, due to the fact that the nanoparticle size in the current experiment model is 15 nm, a separate study was investigated by Maiga et al. [16] to incorporate single phase fluids to study nanofluid behavior and the following correlations for thermal conductivity and dynamic viscosity were utilized:

$$k_r = \frac{k_{nf}}{k_{bf}} = 4.97\varphi^2 + 2.72\varphi + 1$$

$$\mu_r = \frac{\mu_{nf}}{\mu_{bf}} = 123\varphi^2 + 7.3\varphi + 1$$

2.4.4 Limitations

However, with current experiments and results, nanofluids have some significant issues and require much greater analysis to establish a good understanding of its role in heat transfer enhancement. Two of the largest issues with nanofluid analysis involve inconsistency with actual nanofluid development (i.e. nanoparticle immersion, mixing, and suspension) and large disagreement in experimental results with similar setups [11,14]. Standardization of nanoparticle suspension within a base fluid could potentially be a first step in resolving these issues, but requires a great deal of research to understand nanofluid mixture behavior [14].

2.5 “Experimental investigation on heat transfer enhancement due to Al_2O_3 – water nanofluid using impingement of round jet on circular disk” by B. Jaberi, T. Yousefi, B. Farahbakhsh, M.Z. Saghir [2]

This section covers a summary of the results obtained in an experimental study that investigated the heat transfer enhancement associated with the Al_2O_3 – water nanofluid with an impinging jet on a flat circular disk, which will be the validation model for the numerical investigation. Different concentrations of nanoparticles were utilized, from 0.0198 to 0.0757 wt%, while the Reynolds number varied between 4000 and 8200. A number of techniques were utilized to control the agglomeration of the nanoparticles, which included ultrasonic vibration between 60-80%, controlling pH, and adding Sodium Dodecyl Benzene Sulfonate (SDBS) to effectively disperse nanoparticles and avoid agglomeration. Majority of the effects by incorporation of nanofluids were analyzed to give minimum 40% higher heat transfer coefficients for a concentration of 0.0757 wt% for average convective heat transfer coefficients and up to 114.5% for a concentration of 0.0757 wt% at Re = 4052.

3.0 Preliminary Processing and Description of Activities

3.1 Assumptions and Simplifications

Due to the complexity of simulating turbulent flow within an impinging jet, numerous general assumptions and simplifications are outlined below in order to maintain consistency with aspects of the experimental modeling. Properties of the base fluid, nanoparticles, etc. were stated but other variables, such as temperature, were calculated based on various assumptions, which include:

i. heat flux was zero (no heat loss) along the nozzle,
ii. inlet temperature was utilized at the lower end of the given temperature range for all cases (given that the inlet temperature varied for the experiment),
iii. open surfaces/outlet temperatures were room temperature, i.e. 24°C (297.15 K),
iv. constant fluid properties (i.e. density, dynamic viscosity, specific heat capacity, and thermal conductivity) at a specific temperature of 307.15 K (averaged from experimental results), and
v. constant surface properties (i.e. density, specific heat capacity, and thermal conductivity).

These assumptions were done to provide a baseline for further analysis when calculating the heat transfer coefficient for various cases with different Reynolds numbers, H/d ratios, and nanofluid concentrations. Furthermore, experimental data showed that the nanofluid temperature varied between 26°C and 42°C (299.15 K and 315 K) [2], and in order to maintain consistency, the lower end of the range was chosen as the inlet temperature since the actual value for every trial could not be readily obtained.

3.2 Meshing Considerations and Sensitivity Study

The finite element analysis (FEA) software utilized for analysis was ANSYS Fluent and meshing is an extremely important factor as various mesh sizes can produce significant errors in computation or have high computational cost. However, to reduce the potential errors that result from non-convergence or other factors, a mesh sensitivity, or grid independence, study has been conducted in order to obtain the optimal mesh size that requires the least amount of computation cost while providing accurate results within acceptable error margins.

Several mesh sizes were tested with use of the RNG k-ε with enhanced wall treatments turbulence model, which was investigated in a similar numerical study by Jayaraman [6]. A detailed analysis of turbulence models will be investigated in a subsequent section. Overall, the grid independence study will involve primarily analyzing the stagnation point heat transfer coefficient and obtaining an optimal mesh size when the relative error between subsequent meshes is less than 1%. Five mesh changes were tested and examined. Table 3.2.1 below highlights the various mesh sizes, stagnation point heat transfer coefficient, and other parameters useful in analyzing mesh quality, while Figure 3.2.1 below depicted the differences between meshes. Percentage difference was calculated using the following equation:

$$Percentage\ Difference = \frac{|N_1 - N_2|}{\frac{1}{2}(N_1 + N_2)}\ x\ 100$$

Table 3.2.1 – Mesh Sensitivity (Grid Independence) Study Summary

	Mesh Trial				
	1	2	3	4	5
Minimum Mesh Face Size (m) =	0.000001	0.000001	0.000001	0.000001	0.000001
Maximum Mesh Face Size (m) =	0.0015	0.001	0.00075	0.0005	0.00025
Maximum Tet Size (m) =	0.0015	0.001	0.00075	0.0005	0.00025
Number of Elements =	8983	18659	32043	68616	262429
Minimum Orthogonal Quality =	0.782	0.788	0.787	0.803	0.617
Maximum Ortho Skew =	0.218	0.150	0.130	0.197	0.184
Maximum Aspect Ratio =	100.006	6.668	50.011	33.350	16.698
Number of Iterations =	415	731	1028	2080	8333
Current Stagnation Heat Transfer Coefficient (W/m^2K) =	3900.68	3987.17	4011.68	4075.57	4175.67
Next Stagnation Heat Transfer Coefficient (W/m^2K) =	3987.17	4011.68	4075.57	4175.67	-
Stagnation Heat Transfer Coefficient Difference (W/m^2K) =	86.49	24.51	63.89	100.11	-
Percentage Difference (%)	2.19%	0.61%	1.58%	2.43%	-

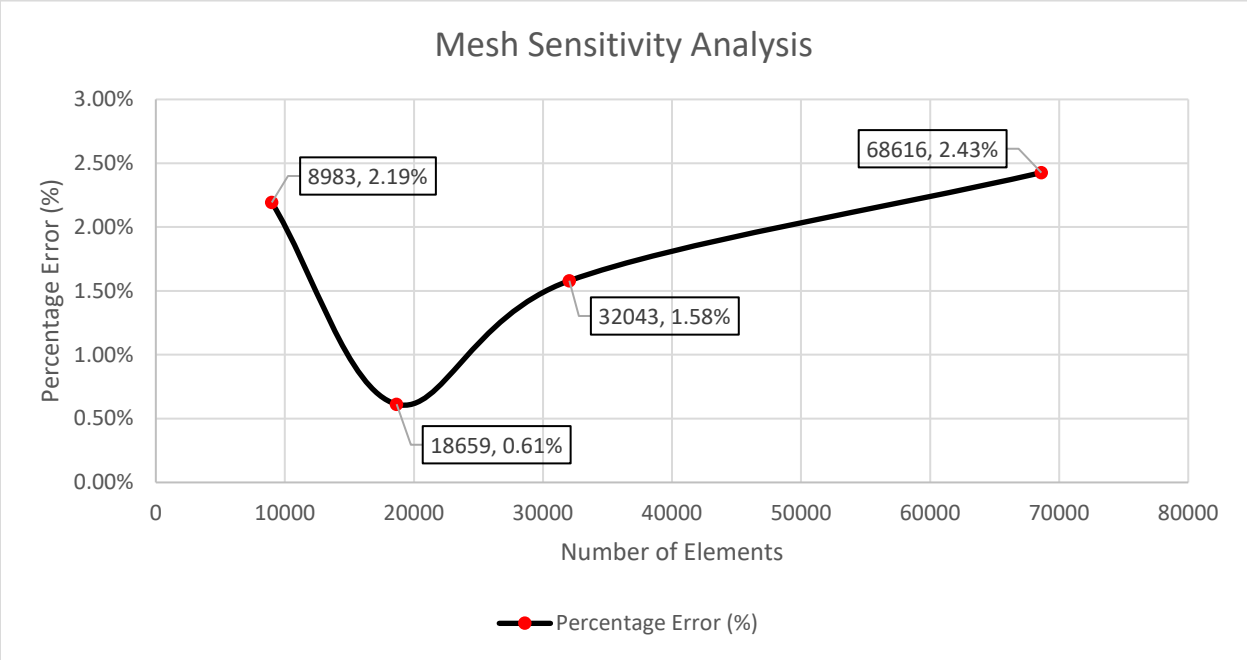

Figure 3.2.1 – Mesh Sensitivity Analysis

Out of the eight meshes tested above, Mesh Trial 2 provided a percentage error that was below 1%, which resulted in its parameters being utilized for the final numerical model. It was able to converge within a reasonable number of iterations, 731, and a total number of elements of 18,659. Majority of the meshing focused primarily on the aluminum surface, and thus a finer mesh was generated at the surface as opposed to other regions in order to resolve boundary layer effects. Mesh quality, i.e. minimum orthogonal quality of 0.788 and maximum ortho skew of 0.150, provided good confidence in supporting convergence of the numerical model. Given that the best mesh quality requires minimum orthogonal quality close to 1 and maximum ortho skew close to 0, it was the best quality mesh developed in comparison to the other mesh trials using the parameters outlined above.

Some of the error associated with the mesh sensitivity analysis involve the overall mesh quality, which influence convergence and stability of the simulation. Generally speaking, given that the mesh was refined at the surface for resolution of the boundary layers, majority of the error occurred from the mesh layers following this region of smaller mesh parameters. Two important characteristics that could have an impact on the error associated with the meshing would be the growth rate and the number of layers with the surface mesh, since they dictate how well the solver can resolve the boundary and viscous sub-layers without resulting in large error when solving various nodes.

Tables 3.2.2 and 3.2.3 outline the various mesh parameters utilized for the model. Physics and Solver preferences were set to CFD and Fluent respectively.

Table 3.2.2 – Mesh Parameters

Parameter	**Value/Condition**
Size Function	Curvature
Relevance Center	Fine
Initial Size Seed	Active Assembly
Smoothing	High
Span Angle Center	Fine
Curvature Normal Angle	Default (18.0°)

Min Size	1.e-006 m
Max Face Size	1.e-003 m
Max Tet Size	1.e-003 m
Growth Rate	1.20
Automatic Mesh Based Defeaturing	On
Defeaturing Tolerance	Default (5e-007 m)
Minimum Edge Length	9.4.e-003 m

Table 3.2.3 – Surface Inflation Mesh Parameters

Parameter	**Value/Condition**
Suppressed	No
Boundary Scoping Method	Geometry Selection
Boundary	1 Edge (Surface)
Inflation Option	First Layer Thickness
First Layer Height	1.5e-005 m
Maximum Layers	10
Growth Rate	1.2
Inflation Algorithm	Pre

Initially, the meshing was refined at the surface for the purpose of resolving boundary layers and viscous sub-layers for turbulence and viscous effects [6], which depending on the Reynolds number utilized, can affect the required sizing. For resolving the boundary layer and its viscous sub-layers, a wall y-plus, or y^+, of less than or equal to 1 was utilized in order to obtain accurate heat transfer coefficient values at locations close to the impingement surface. The first layer thickness method was utilized to estimate the first layer height and a subsequent number of layers needed for resolution. The following equation was utilized to determine the required y^+ value of less than or equal to 1, which was obtained from Fluid Mechanics, 5th Edition by Frank M. White [17] with some modification:

$$\Delta s = \frac{y^+ \mu}{U_{friction} \rho}$$

Rearranging and testing the largest Reynolds number in this numerical study (10,000), the first layer thickness was determined to be approximately 1.6 x 10^{-5} m for a desired y^+ value of less than or equal to 1. Figures 3.2.2 and 3.2.3 depict the developed mesh and the boundary layer resolution respectively.

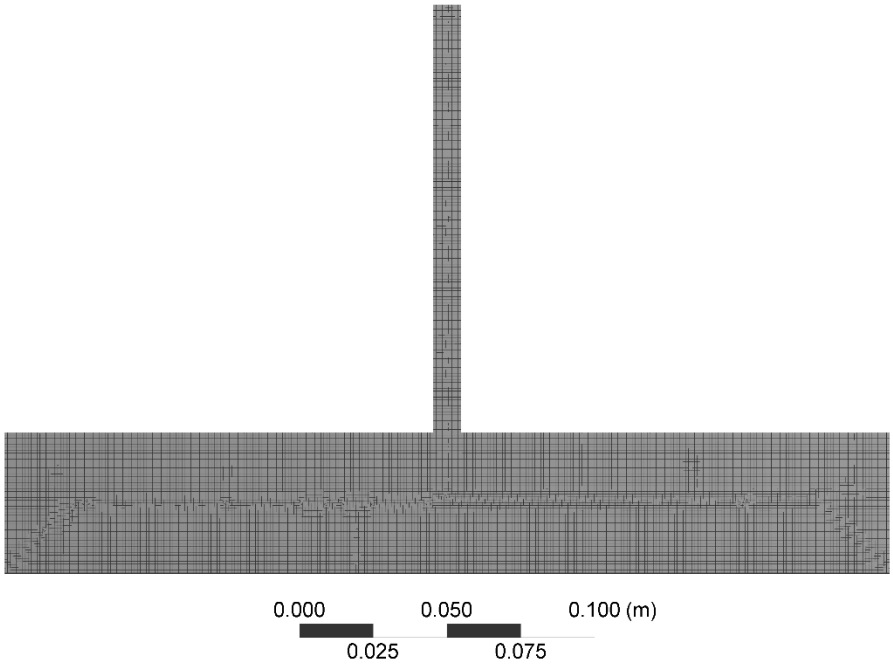

Figure 3.2.2 – 2D Model Meshing

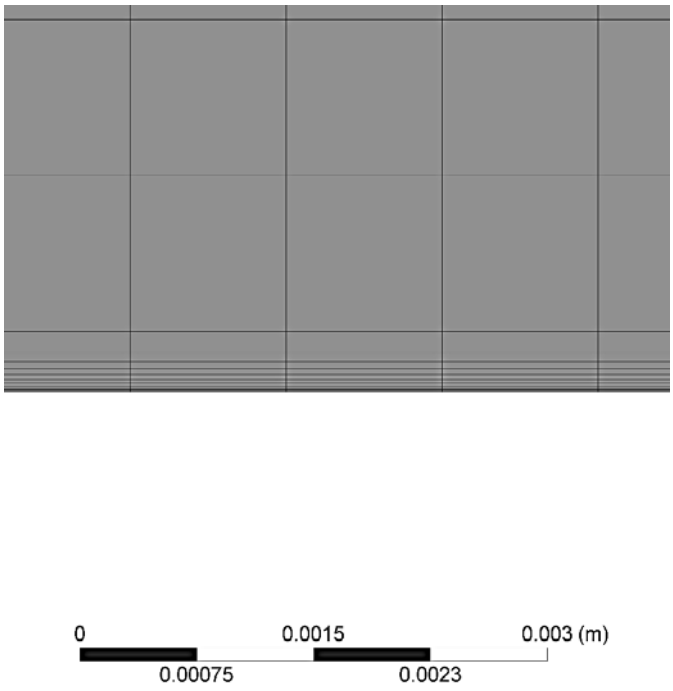

Figure 3.2.3 – Surface Boundary Layer Mesh Resolution

3.3 Modeling Parameters, Properties, and Boundary Conditions

After developing the mesh and the respective inlet, outlets, etc., the material properties and boundary conditions were obtained from the experimental study by B. Jaberi et al. [2]. Various properties for the fluid, surface, nanoparticle, and nanofluid are presented in Tables 3.3.1 to 3.3.4 with interpolated data respectively, along with the boundary conditions outlined in Table 3.3.5.

Table 3.3.1 – Fluid (Water) Properties [2]

Property	**Value/Condition**
Average Temperature, T_f (K)	307.15
Density, ρ_f (kg/m^3)	993.86
Dynamic Viscosity, μ_f (Ns/m^2)	7.44 x 10^{-4}
Specific Heat Capacity, $c_{p,f}$ (J/kgK)	4175.14
Thermal Conductivity, k_f (W/mK)	0.623

Table 3.3.2 – Surface (Aluminum) Properties [2]

Property	**Value/Condition**
Density, ρ_s (kg/m^3)	2702
Specific Heat Capacity, $c_{p,s}$ (J/kgK)	903
Thermal Conductivity, k_s (W/mK)	237

Table 3.3.3 – Nanoparticle (Al_2O_3) Properties [2]

Property	**Value/Condition**
Density, ρ_{np} (kg/m^3)	3890
Specific Heat Capacity, $c_{p,np}$ (J/kgK)	880
Thermal Conductivity, k_{np} (W/mK)	35

The nanofluid properties were determined through the use of the correlations outlined in section 2.4.3, which are as follows:

$$\rho_{nf} = \left(1 - \frac{\phi}{100}\right)\rho_{bf} + \left(\frac{\varphi}{100}\right)\rho_{np}$$

$$c_{p,nf} = \frac{\frac{\varphi}{100}\left(\rho c_p\right)_{np} + \left(1 - \frac{\varphi}{100}\right)\left(\rho c_p\right)_{bf}}{\rho_{nf}}$$

$$k_r = \frac{k_{nf}}{k_{bf}} = 4.97\varphi^2 + 2.72\varphi + 1$$

$$\mu_r = \frac{\mu_{nf}}{\mu_{bf}} = 123\varphi^2 + 7.3\varphi + 1$$

However, given that there are four different concentrations of Al_2O_3-H_2O that were tested, each concentration will have its own properties dependent on the equations shown above. However, a conversion must be applied to the concentrations to convert from weight % to volume %, in order to the correlations shown above to be valid (solute and solvent are nanoparticle and water respectively),

$$wt\% = \frac{w_{solute}}{w_{solvent}} x100 = \frac{(\rho V)_{solute}}{(\rho V)_{solvent}} x100$$

$$\left(\frac{V_{solute}}{V_{solvent}}\right) x100 = wt\% \left(\frac{\rho_{solvent}}{\rho_{solute}}\right)$$

By definition,

$$vol\% = \left(\frac{V_{solute}}{V_{solvent}}\right) x100 \rightarrow vol\% = wt\% \left(\frac{\rho_{solvent}}{\rho_{solute}}\right)$$

Table 3.3.4 – Nanofluid (Al_2O_3-Water) Properties [2]

Concentration (wt%) =	0.0198	0.0353	0.0597	0.0757
Concentration (vol%) =	0.0051	0.0090	0.0153	0.0193
Density, ρ_{nf} (kg/m^3) =	994.00	994.12	994.30	994.42
Specific Heat Capacity, $c_{p,nf}$ (J/kgK) =	4174.49	4173.98	4173.17	4172.65
Thermal Conductivity, k_{nf} (W/mK) =	0.63181	0.63869	0.64973	0.65710
Dynamic Viscosity, μ_{nf} (Ns/m^2) =	0.0007738	0.000800	0.0008482	0.000883

Table 3.3.5 – Summary of Boundary Conditions [2]

Boundary Condition	**Type**	**Subcategory**	**Value/Parameter**
Inlet	Velocity Inlet	Momentum	U = Various ($2000 \leq Re \leq 10{,}000$)
		Thermal	T = 299.15 K
Adiabatic Walls	Wall	Momentum	Stationary Wall, No Slip
		Thermal	Heat Flux = 0 W/m^2
Outlets	Pressure Outlet	Momentum	P = 0 Pa
		Thermal	T = 297.15 K
Surface	Wall	Momentum	Stationary Wall, No Slip
		Thermal	Heat Flux = 11590/17580 W/m^2 (Re = 4245.7/8282)

Note: specific boundary conditions were chosen based on previously made assumptions. The outlet boundaries were assumed to be at room temperature of 24°C, while the inlet temperature was taken to be at the lower end of the given temperature range and inlet velocities was calculated at the averaged fluid temperature for properties. Additionally, given that several Reynolds numbers were tested (i.e. 2000, 4245.7, 6000, 8282, 10000), the heat flux boundary condition was adjusted accordingly in that Reynolds numbers below and above 8282 were assigned heat flux boundary conditions of 11590 W/m^2 and 17580 W/m^2, respectively, in order to maintain consistency with experimental data.

The solver setup included applying a pressure-based, absolute velocity formation, steady-state, planar solver system with gravitational effects. In addition, the energy model and viscous SST k-ω turbulence model were activated, which will be discussed in a subsequent section. For solution methods, the pressure-velocity coupling scheme was used as SIMPLE, with momentum, turbulent kinetic energy, specific dissipation rate, and energy as second order upwind to increase accuracy of results [3]. Moreover, the residual monitors of continuity, x-y velocities, k, and omega were set to an absolute criterion of 1×10^{-4}, while energy was set to 1×10^{-6}. These particular values were selected to reduce error and instability in the modeling [3]. Hybrid initialization computing was utilized and the simulation was completed.

A total of 75 simulations were run (5 fluids, 5 Reynolds numbers, 3 H/d ratios), which include the several modifications completed after validation of results.

4.0 Numerical Simulation Results and Validation

4.1 Turbulence Model Optimization and Selection

Several turbulence models were investigated with respect to scholarly sources and other studies in order to select an optimal and accurate turbulence model to predict the behavior of the impinging jet. This investigation involved researching for information pertaining to turbulence models such as the k-ε, k-ω, Transition k-kl-ω, v^2f, etc. with H_2O as the working fluid. After several simulations, testing, and validation, the SST k-ω turbulence model provided decently good results due to its ability to analyze highly transitional flows occurring at the stagnation region, along with good predictability of viscous sub-layer characteristics. Out of several turbulence models, the SST k-ω turbulence model provided the lowest maximum percentage error with respect to the data for water (H_2O) outlined in the primary experimental paper. It also provided the second-lowest average percentage error of 0.67% higher than the Transition SST turbulence model. Each turbulence model was run with identical parameters for a Reynolds number of 4245.7, inlet velocity of 0.3381 m/s (calculated given the density and dynamic viscosity of H_2O at averaged values), inlet temperature of 299.15 K, impingement surface heat flux of 11590 W/m^2 and diameter of the nozzle of 0.0094 m. Additionally, the bulk temperature required for calculation of the heat transfer coefficient was determined through the mass-weighted averaged surface integral for total temperature. Figures 4.1.1 and 4.1.2 display the experimental heat transfer coefficient values with respect to the numerical result using various turbulence models and their overall predicted trends.

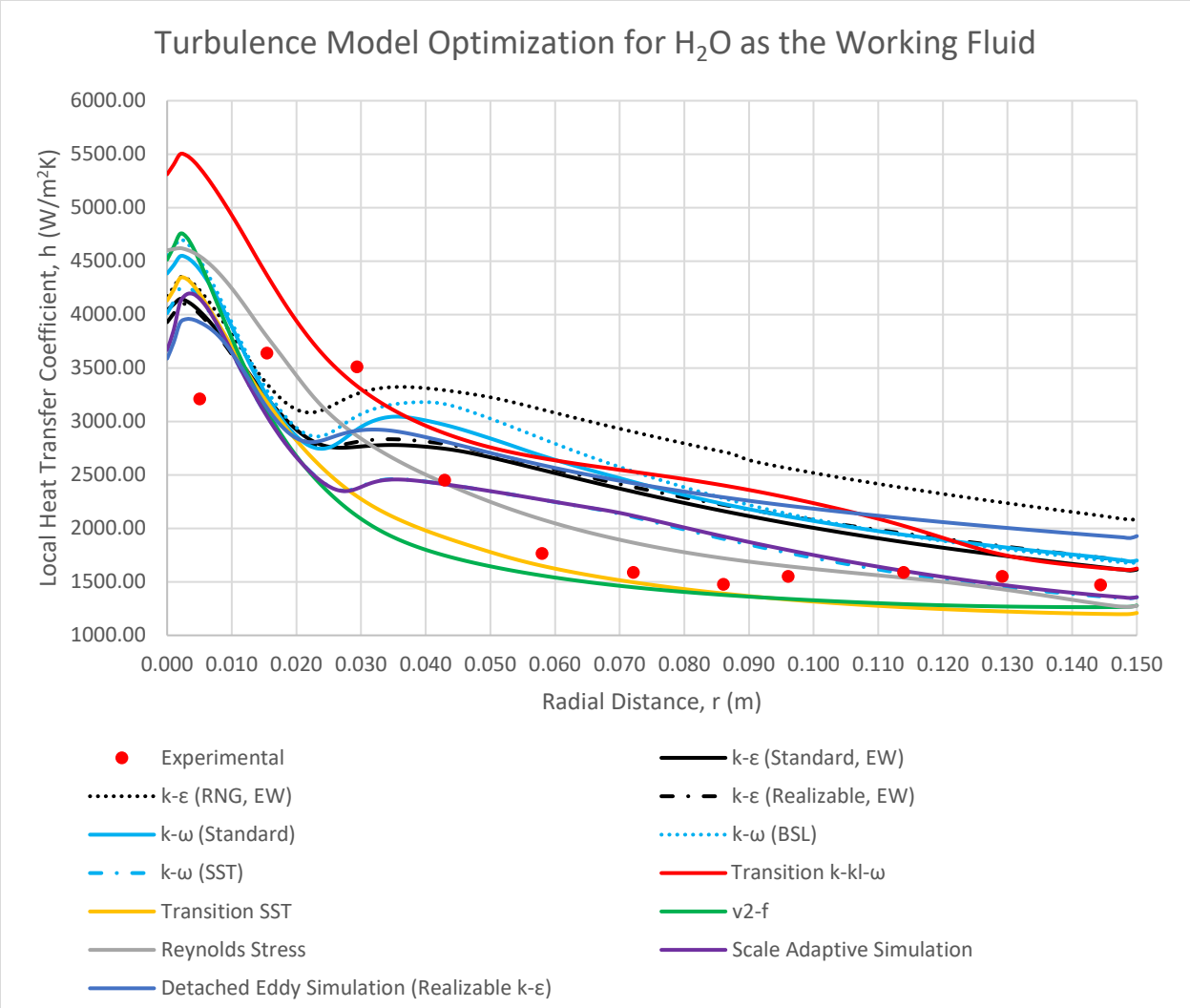

Figure 4.1.1 – Turbulence Model Optimization for H_2O as the Working Fluid

Overall, the SST k- ω turbulence model provided good characteristics for resolving severe pressure gradients along with flow separation, which promotes its use with impinging jets [3]. Other factors that make it a good candidate as a turbulence model include decent predictability of position and magnitude of the second peak, with the offset of low computational cost [3]. However, errors of at least 10-30% are expected to occur given the complexity of the flow [3].

Other advanced turbulence models, such as the Reynolds Stress, Scale Adaptive Simulation, and Detached Eddy Simulations, initially had issues with convergence and relaxation factors were adjusted constantly to achieve convergence, but did not necessarily provide fully converged solutions due to the extremely high computational cost, which was not a feasible solution for

commercial, affordable computers and processors. Some estimates of the time required for solutions were up to 40 hours for the Reynolds Stress, and more complex models required computational times as high as several weeks [3]. Figure 4.1.2 displays the three turbulence models (SST k- ω, Transition SST, and Scale Adaptive Simulation) that produce error under 35% out of all turbulence models tested.

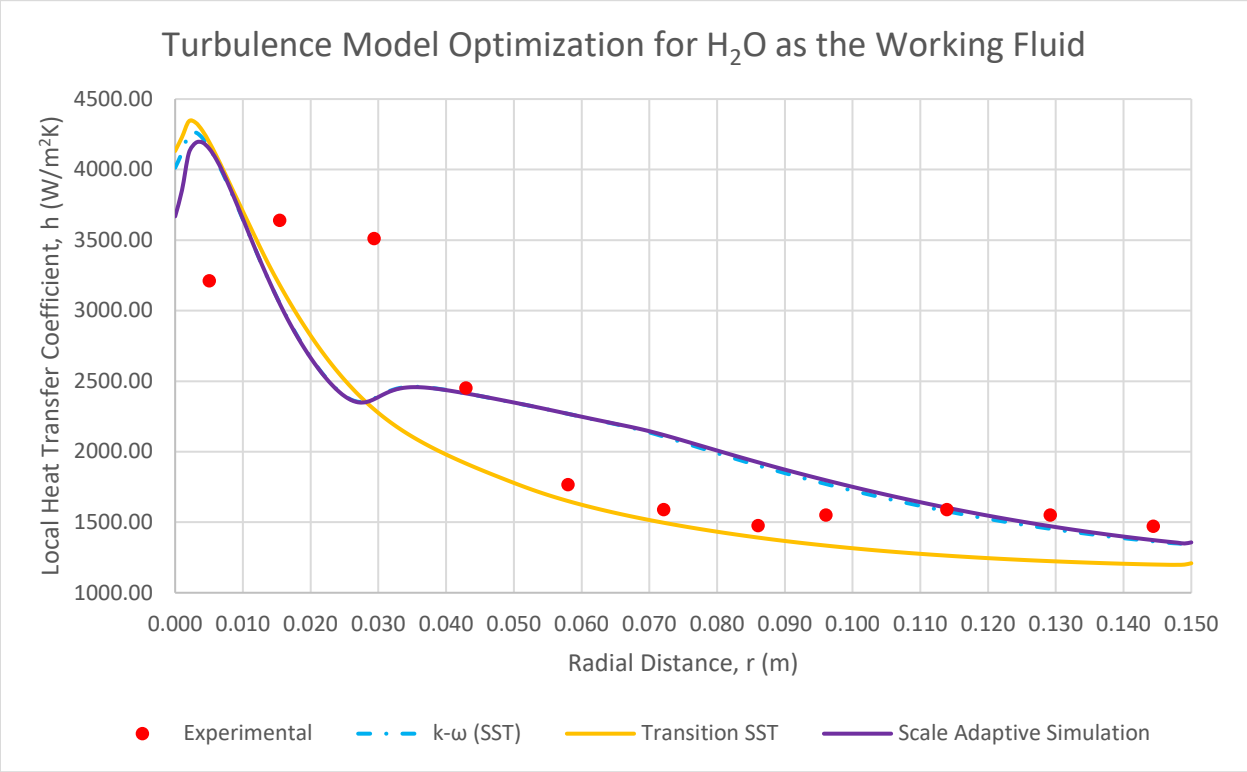

Figure 4.1.2 – Lowest Percentage Error Turbulence Models

Tables 4.1.1 to 4.1.4 below highlight the various percentage errors between the experimental data and the various turbulence models of the numerical model. Percentage error was calculated using the following equation:

$$Percent\ Error\ (\%) = \left|\frac{Experimental - Numerical}{Experimental}\right| x\ 100$$

Table 4.1.1 – Experimental Data [2]

r (m)	Local Heat Transfer Coefficient for H_2O
0.005	3212.24
0.015	3639.89
0.029	3511.38
0.043	2451.14
0.058	1766.63
0.072	1589.02
0.086	1476.57
0.096	1551.54
0.114	1589.02
0.129	1551.54
0.144	1471.22

Table 4.1.2 – Turbulence Model Optimization for H_2O as the Working Fluid at Re = 4245.7

	Percentage Errors (%)					
r (m)	k-ε (Standard, EW)	k-ε (RNG, EW)	k-ε (Realizable, EW)	k-ω (Standard)	k-ω (BSL)	k-ω (SST)
0.005	25.51	31.62	24.66	37.58	40.45	29.39
0.015	10.78	7.22	12.43	10.03	8.67	15.23
0.029	21.33	7.31	20.04	16.90	13.30	32.42
0.043	12.71	35.06	14.66	22.64	29.76	0.63
0.058	43.84	75.81	45.88	51.25	60.19	28.17
0.072	47.14	82.36	49.94	52.85	58.92	32.28
0.086	46.83	84.34	50.72	51.37	55.05	29.28
0.096	32.23	65.45	36.59	36.36	38.01	14.48
0.114	17.89	49.81	23.00	22.22	21.98	0.61
0.129	12.74	44.71	18.34	17.83	16.82	6.17
0.144	11.52	44.24	17.54	17.59	16.12	7.10

Table 4.1.3 – Turbulence Model Optimization for H_2O as the Working Fluid at Re = 4245.7 (C.)

	Percentage Errors (%)					
r (m)	**Transition k-kl-ω**	**Transition SST**	**V^2-f**	**Reynolds Stress**	**Scale Adaptive Simulation**	**Detached Eddy Simulation (Realizable k-ε)**
0.005	67.22	30.58	39.95	41.52	29.15	22.27
0.015	20.97	11.79	13.88	4.97	15.30	13.21
0.029	4.89	34.28	39.52	18.17	32.55	17.06
0.043	20.49	19.47	26.78	1.80	0.67	16.26
0.058	50.16	6.90	11.97	17.53	28.18	46.43
0.072	59.01	6.04	8.91	17.16	33.01	52.22
0.086	63.03	5.57	6.54	16.84	30.81	55.44
0.096	47.76	13.85	13.51	6.27	16.18	42.79
0.114	27.56	20.48	18.66	3.12	0.98	31.87
0.129	13.40	21.07	18.13	7.60	4.98	29.55
0.144	11.06	18.38	14.11	11.87	6.51	31.48

Table 4.1.4 – Average and Maximum Percentage Errors for H_2O as the Working Fluid

Turbulence Model	**Average Error (%)**	**Maximum Error (%)**
k-ε (Standard, EW)	25.68	47.14
k-ε (RNG, EW)	47.99	84.34
k-ε (Realizable, EW)	28.53	50.72
k-ω (Standard)	30.60	52.85
k-ω (BSL)	32.66	60.19
k-ω (SST)	17.80	32.42
Transition k-kl-ω	35.05	67.22
Transition SST	17.13	34.28
v2-f	19.27	39.95
Reynolds Stress	13.35	41.52
Scale Adaptive Simulation	18.03	33.01
Detached Eddy Simulation (Realizable k-ε)	32.60	55.44

4.2 Analysis of the Local Heat Transfer Coefficient Variation with Radial Distance for Reynolds Numbers of 4245.7 and 8282

With respect to Fig. 7 and Fig. 8 in the experimental study by B. Jaberi et al. [2], the experimental results were obtained using plot extraction software in order to establish and compare experimental and numerical results. After completing two particular simulations utilizing the geometric properties previously outlined with Reynolds numbers of 4245.7 and 8282, several results were obtained and provided some insight into the overall flow and heat transfer characteristics. From these two simulations, it can be determined that the percentage error generally increases with increasing Reynolds number as shown in Figure 4.2.1 and 4.2.2, which could be due to a number of assumptions and/or limitations in the modeling. Due to these largely varying results, certain parameters will likely need to be investigated in order to establish an accurate numerical model. Figures 4.2.3 and 4.2.4 display the experimental and numerical data for Reynolds numbers of 4245.7 and 8282 (experimental = dot, numerical = line). It is evident that the contribution of the nanoparticles to the overall thermal characteristics of the nanofluid is rather significant in the numerical model, which is influenced by a combination of factors, such as the bulk temperature determination by the numerical software, the turbulence model limits, etc.

It was observed that one specific phenomena occurred to produce higher local heat transfer coefficients for Reynolds number of 4245.7 but not for 8282, which involves the wall jet region of fluid flow. This is due to the fact that at lower Reynolds numbers, the nanofluid mixture has significant turbulent mixing occurring around 0.100 m, which allows for higher local heat transfer coefficients due to the high thermal conductivity of the nanoparticles. However, at higher Reynolds numbers, the same turbulent mixing effect does not produce the same local heat transfer coefficient increase given that the nanofluid has increased velocity across the surface, and thus, does not allow the formation of the second peak in the wall jet region due to shortened periods of time for heat transfer to occur among nanoparticles. As described in the experimental study by B. Jaberi et al. [2], the hydraulic jump was a result of the flow changing from supercritical to subcritical. However, this was not present in the numerical simulation given several assumptions made initially along with other factors described in a later section.

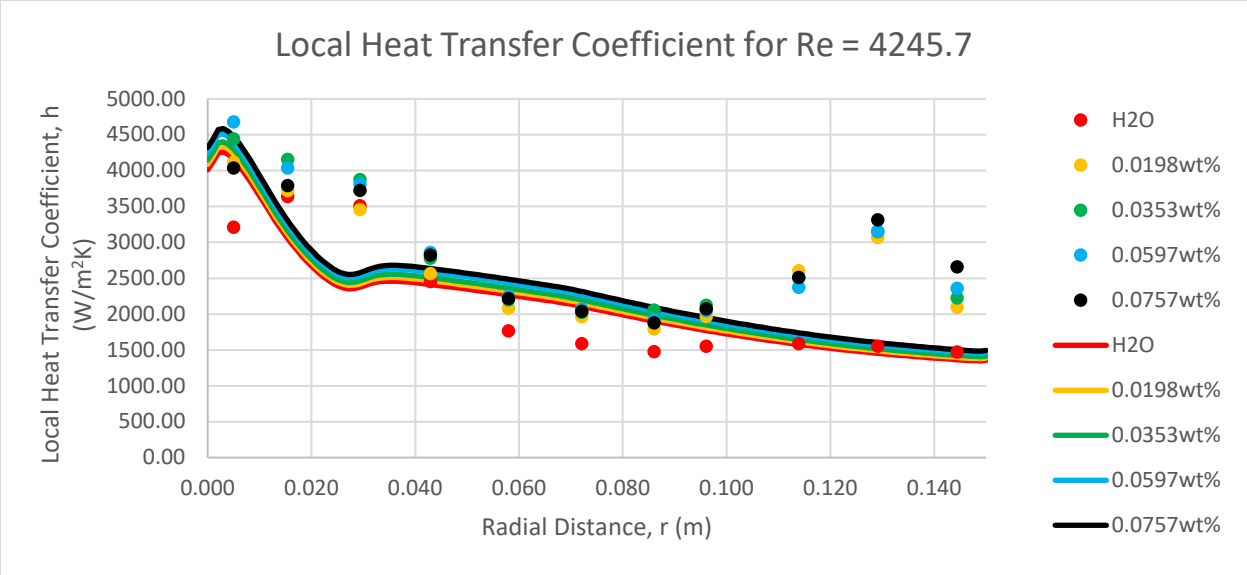

Figure 4.2.1 – Local Heat Transfer Coefficient for Re = 4245.7

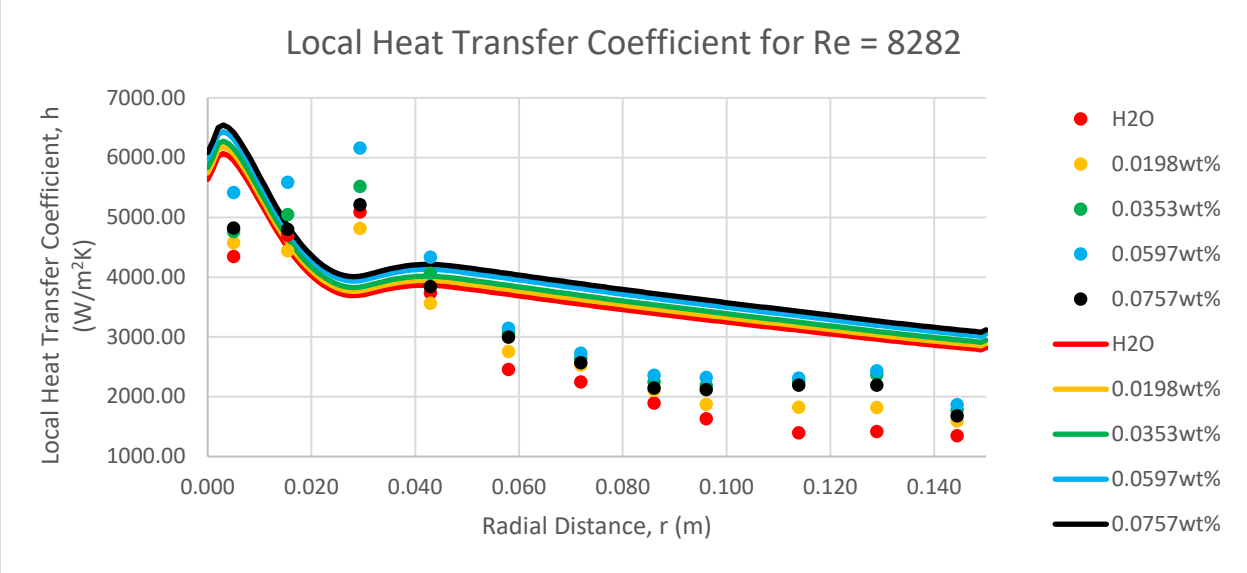

Figure 4.2.2 – Local Heat Transfer Coefficient for Re = 8282

Tables 4.2.1 and 4.2.2 displays the experimental heat transfer coefficients values required for validation, while Tables 4.2.3 and 4.2.4 display numerical heat transfer coefficient values and percentage errors between experimental and numerical results. Figures 4.2.3 and 4.2.4 display the range of percentage errors against the radial distance.

Table 4.2.1 – Experimental Data for Re = 4245.7

	Local Heat Transfer Coefficient (W/m^2K)				
r (m)	**H_2O**	**0.0198wt%**	**0.0353wt%**	**0.0597wt%**	**0.0757wt%**
0.005	3212.24	4116.47	4444.70	4678.71	4038.94
0.015	3639.89	3718.31	4159.30	4035.11	3790.68
0.029	3511.38	3455.13	3874.69	3815.19	3726.75
0.043	2451.14	2563.61	2777.78	2858.10	2822.10
0.058	1766.63	2084.23	2199.46	2247.66	2215.53
0.072	1589.02	1963.86	2023.02	2070.95	2038.82
0.086	1476.57	1792.50	2057.19	1921.02	1878.21
0.096	1551.54	1968.72	2124.50	2047.41	2076.31
0.114	1589.02	2603.63	2506.56	2373.47	2512.27
0.129	1551.54	3066.93	3147.26	3157.97	3313.25
0.144	1471.22	2097.46	2226.52	2357.70	2656.56

Table 4.2.2 – Experimental Data for Re = 8282

	Local Heat Transfer Coefficient (W/m^2K)				
r (m)	**H_2O**	**0.0198wt%**	**0.0353wt%**	**0.0597wt%**	**0.0757wt%**
0.005	4347.68	4573.40	4761.50	5417.98	4819.55
0.015	4698.59	4439.18	5044.30	5585.04	4798.14
0.029	5090.26	4814.50	5518.04	6159.29	5210.64
0.043	3734.11	3561.63	4068.21	4336.59	3840.01
0.058	2454.19	2755.15	3063.59	3146.39	2994.61
0.072	2249.73	2531.86	2648.50	2731.27	2567.74
0.086	1894.78	2105.45	2248.41	2357.23	2147.13
0.096	1630.50	1872.84	2187.27	2322.81	2119.56
0.114	1396.64	1824.28	2251.35	2313.50	2191.01
0.129	1416.74	1816.86	2369.52	2434.65	2191.70
0.144	1348.84	1591.66	1776.43	1868.22	1678.55

Table 4.2.3 – Percentage Errors for Re = 4245.7

	Percentage Error (%)				
r (m)	**H_2O**	**0.0198wt%**	**0.0353wt%**	**0.0597wt%**	**0.0757wt%**
0.005	29.332	2.758	3.397	5.948	10.787
0.015	15.262	15.466	23.231	18.791	12.006
0.029	32.437	29.970	36.503	33.756	30.922
0.043	1.694	3.978	9.777	9.698	6.691
0.058	28.134	11.028	7.187	8.135	12.003
0.072	32.245	9.414	8.303	9.133	13.249
0.086	29.257	8.909	3.193	6.972	11.826
0.096	14.460	7.717	12.748	6.538	5.783
0.114	0.632	37.941	34.219	28.262	30.704
0.129	6.188	51.432	51.706	50.295	51.562
0.144	7.113	33.331	35.919	37.508	43.293
Average =	17.887	19.268	20.562	19.549	20.802

Table 4.2.4 – Percentage Errors for Re = 8282

	Percentage Error (%)				
r (m)	**H_2O**	**0.0198wt%**	**0.0353wt%**	**0.0597wt%**	**0.0757wt%**
0.005	36.785	32.429	29.162	16.377	33.100
0.015	3.545	4.060	6.954	13.739	2.222
0.029	27.404	21.701	30.533	36.051	22.979
0.043	3.504	10.801	1.281	4.707	9.743
0.058	51.018	37.450	25.884	26.269	35.405
0.072	57.396	42.959	39.247	39.210	51.208
0.086	79.327	65.027	57.498	54.969	73.801
0.096	101.946	79.836	56.982	52.541	70.823
0.114	122.858	74.605	44.290	45.007	56.529
0.129	109.153	66.964	30.603	31.320	49.194
0.144	109.723	81.990	66.381	63.514	86.197
Average =	63.878	47.075	35.347	34.882	44.655

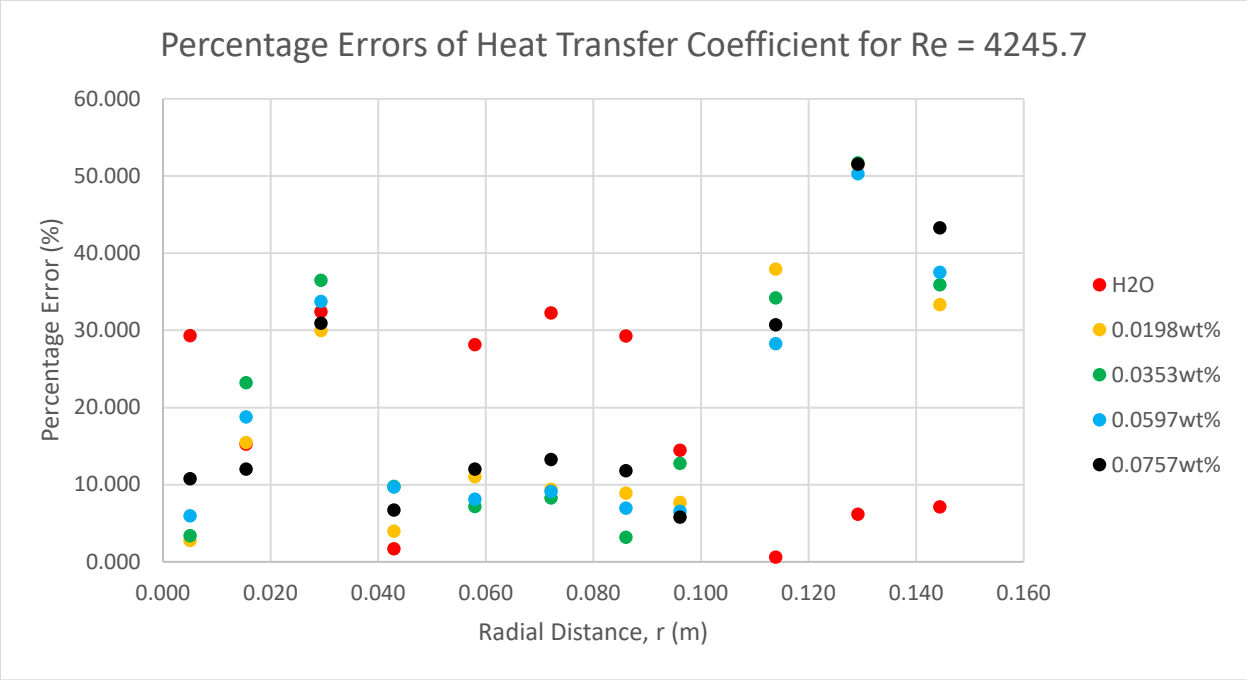

Figure 4.2.3 - Percentage Errors for Re = 4245.7

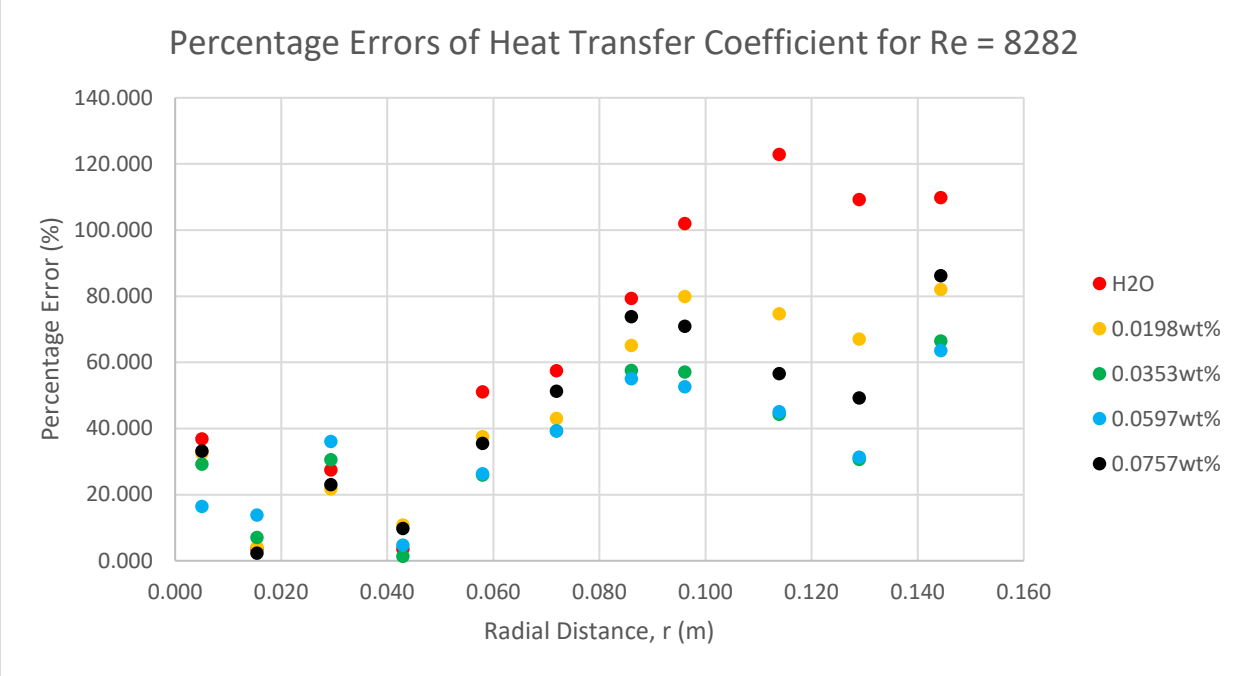

Figure 4.2.4 - Percentage Errors for Re = 8282

From Tables 4.2.3 and 4.2.4 and Figure 4.2.1 and 4.2.2, it is evident that for a Reynolds number of 4245.7, the percentage errors between experimental and numerical results are reasonably decent, with averages for H_2O at 17.887% and across all concentrations reaching a maximum of 20.802%, given that typical good turbulence models provide errors between 2-30% as highlighted by Zuckerman & Lior [3]. However, for a Reynolds number of 8282, the percentage errors between experimental and numerical results have far greater error percentages, with averages for H_2O at 63.878% and across all concentrations reaching a maximum of 47.075%, It can be witnessed that several outliers of numerical data typically occur at increasing radial distance for the base fluid and several concentrations of nanofluid, which is possibly due to some of the assumptions, such as constant thermal properties, that influence the results greatly. These errors will be discussed in a subsequent section.

4.3 Analysis of the Average Heat Transfer Coefficient Variation for Reynolds Numbers of 4245.7 and 8282

With respect to Fig. 10 in the experimental study by B. Jaberi et al. [2], the experimental results were obtained using plot extraction software in order to establish and compare experimental and numerical results. Figure 4.3.1 below depicts the various experimental (shaded black and white) and numerical (various colors) results. It can be ascertained that the percentage error is relatively small for low Reynolds numbers (~4200) but increases greatly for higher Reynolds numbers (~8200), which is due to several initial assumptions in modeling (i.e. constant thermal properties). Percentage errors were not necessarily calculated given the fact that the Reynolds numbers for experimental data was not explicitly 4245.7 and 8282 (chosen for the numerical model).

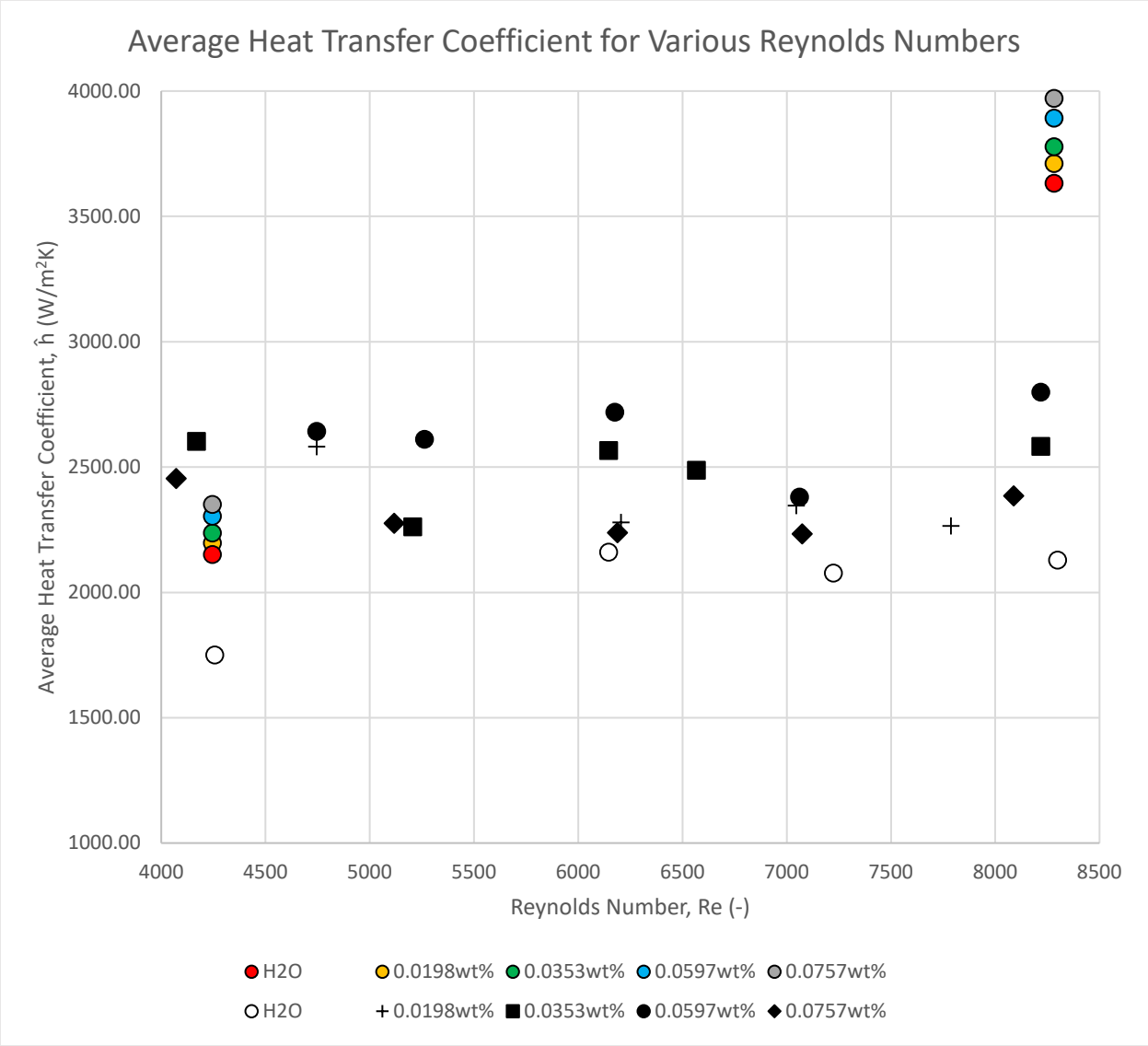

Figure 4.3.1 – Average Heat Transfer Coefficient for Various Reynolds Numbers

4.4 Analysis of the Velocity and Pressure Profiles

In the post-processing stage of the results, the velocity profiles for both Reynolds numbers of 4245.7 and 8282, as shown in Figures 4.4.1 to 4.4.4, coincide with the literature review and the overall flow structure present in the impinging jet. Each of the three main regions of interest, i.e. free jet, stagnation, and wall jet regions were accurately depicted in both simulations. Additionally, the pressure profiles for both Reynolds numbers of 4245.7 and 8282, as shown in Figure 4.4.5 and 4.4.6, are indicative of the high pressures that occur primarily at the stagnation region. However, because the dimensionless jet height-to-jet diameter (H/d) ratio was approximately 5.11, the current simulations did not depict a pronounceable or evident second peak, which is known to occur for smaller H/d ratios, which are investigated in a subsequent section.

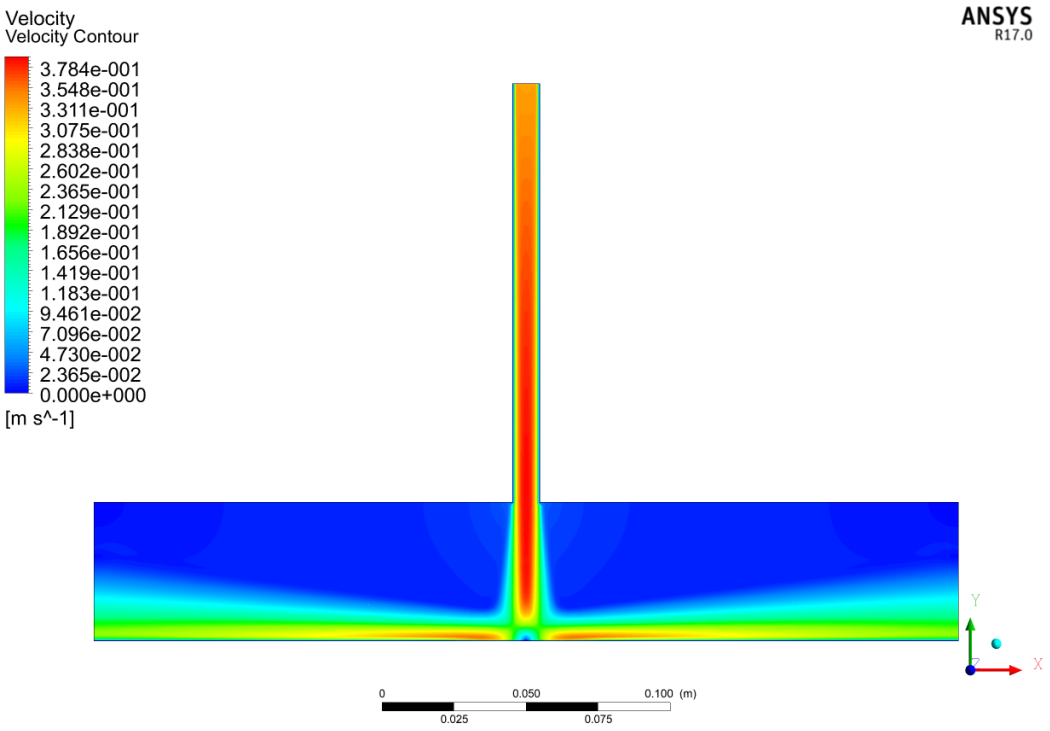

Figure 4.4.1 – Velocity Profile for Re = 4245.7

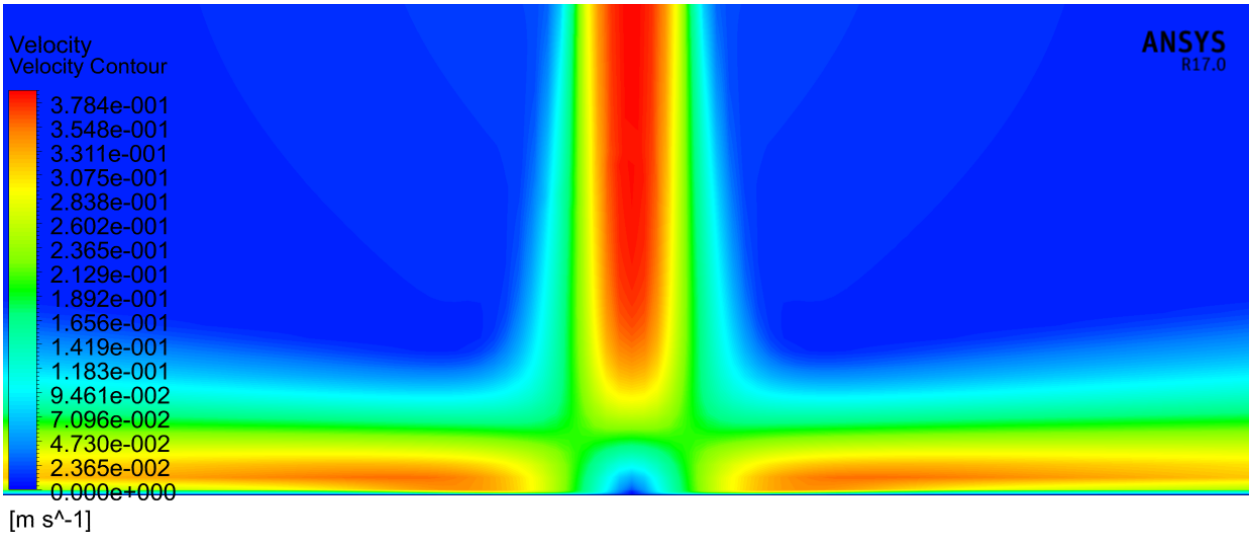

Figure 4.4.2 – Stagnation Region Velocity Profile for Re = 4245.7

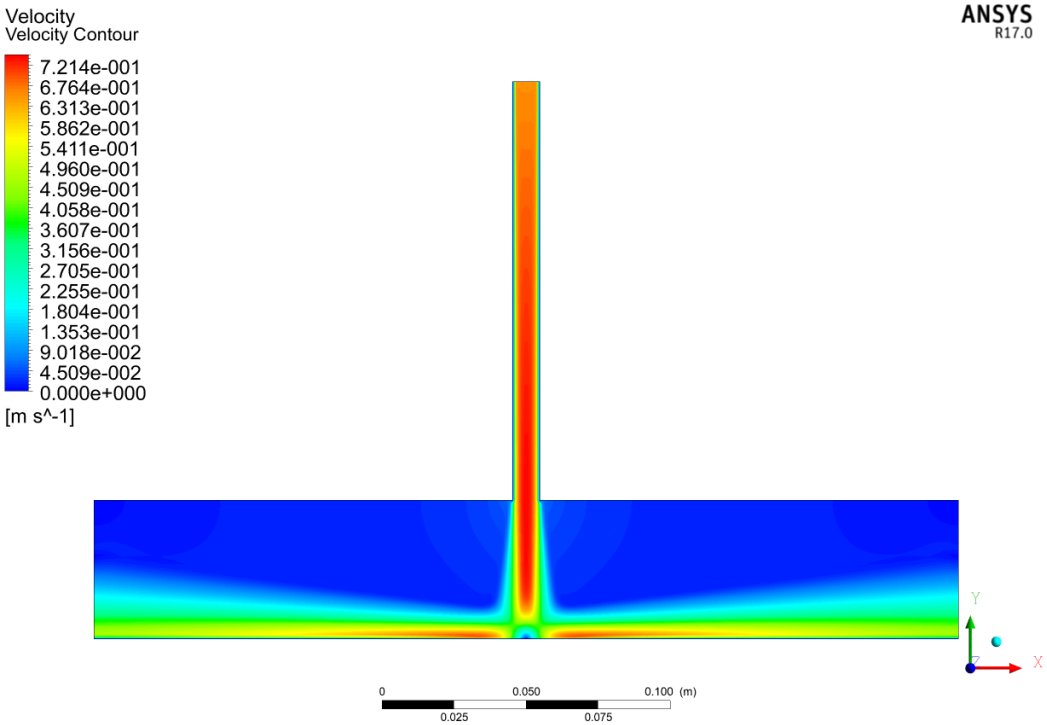

Figure 4.4.3 – Velocity Profile for Re = 8282

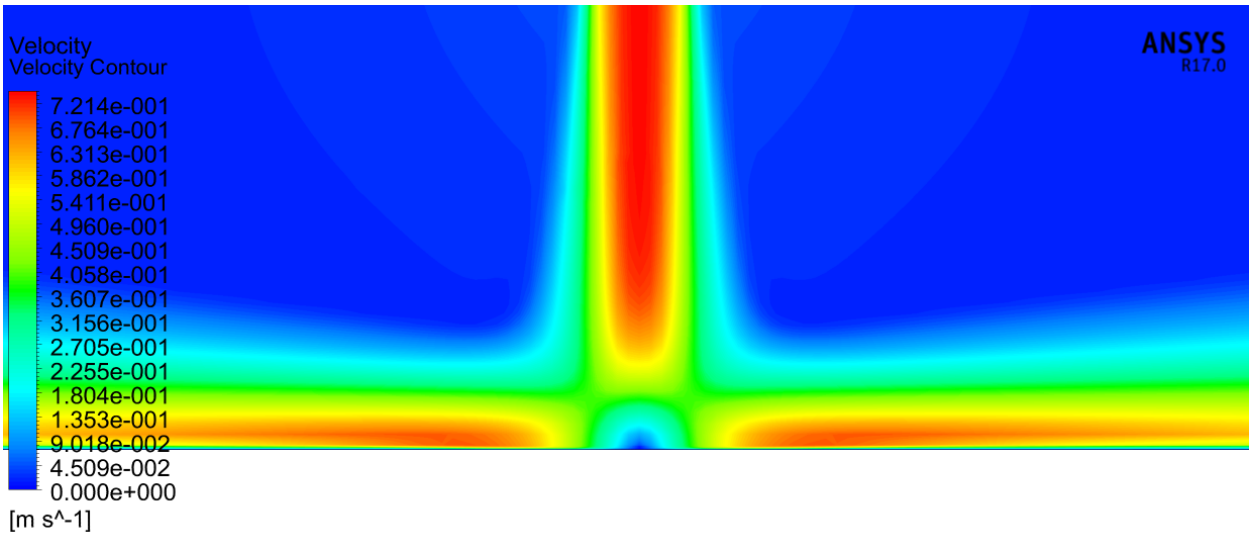

Figure 4.4.4 – Stagnation Region Velocity Profile for Re = 8282

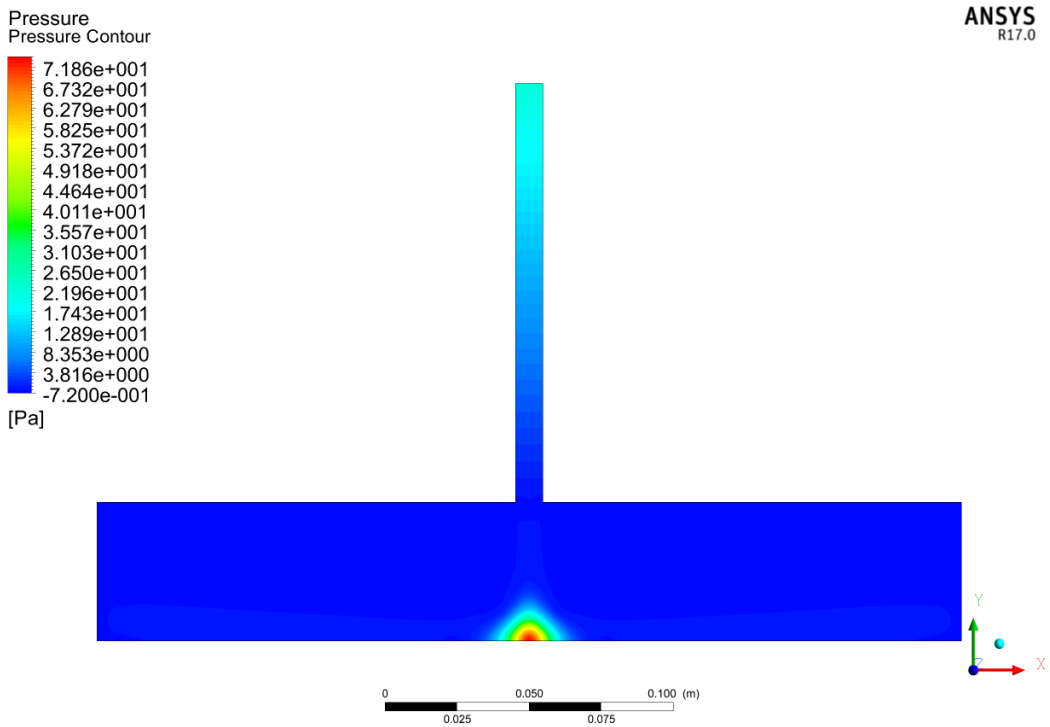

Figure 4.4.5 – Pressure Profile for Re = 4245.7

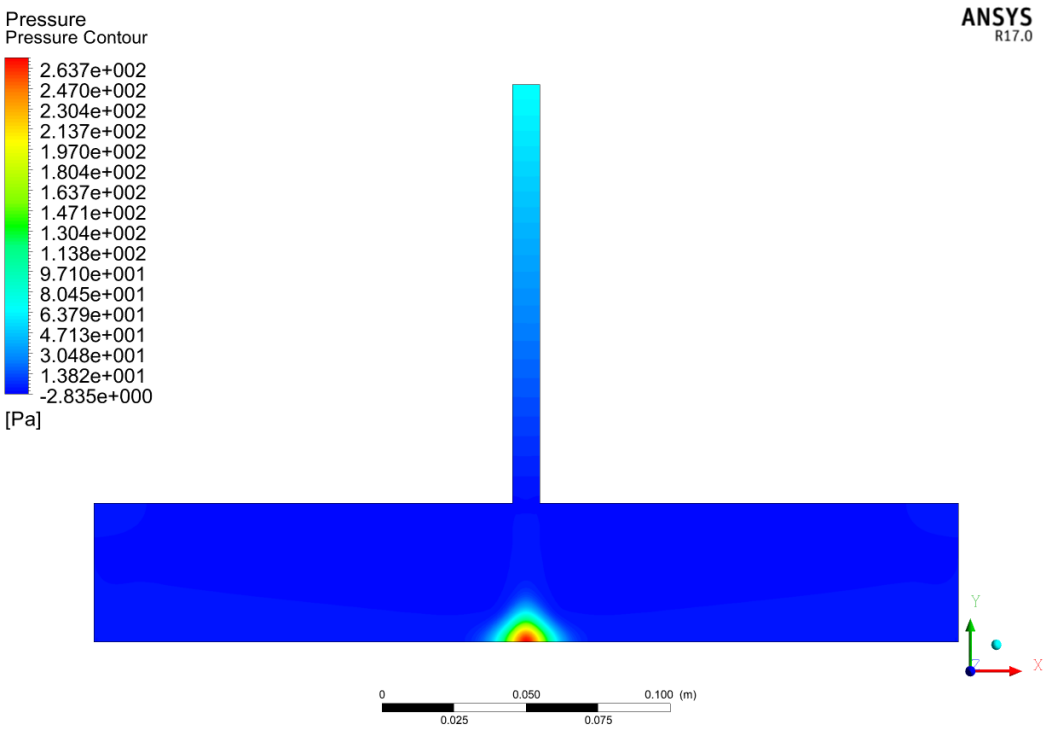

Figure 4.4.6 – Pressure Profile for Re = 8282

5.0 Additional Analysis

In accordance with the project requirements, other adjustments were made to the numerical model to investigate the effect of changing the Reynolds number and jet height-to-jet diameter (H/d) ratio. This section of the report involves analyzing 5 different Reynolds numbers of 2000, 4245.7 (experiment), 6000, 8282 (experiment), and 10000, along with 3 different H/d ratios of 2, 5.11 (experiment), and 10. Each of the nanofluid concentrations, along with the base fluid H_2O, were tested with these parameters.

5.1 Analysis of the Average Heat Transfer Coefficient for Various Reynolds Numbers and H/d Ratios

Figure 5.1.1 and 5.1.2 depict the average heat transfer coefficient for various Reynolds Numbers and H/d ratios mentioned previously. It can be identified that the trends are consistent for various concentrations of nanofluid and base fluid of water. What is important to note is that the maximum average heat transfer coefficient occurs at a Reynolds number of approximately 6000 and H/d ratio of 2. Naturally, decreasing the H/d ratio increases the overall average heat transfer coefficient as proven in this particular study, where the maximum difference between respective H/d ratios occurs at approximately at a Reynolds number of ~6300. However, at a Reynolds number of approximately >8500, it can be seen that the average heat transfer coefficient for H/d ratio of 10 surpasses that of 5.11, which could be accounted for given that the length of the potential core is much larger for larger H/d ratios, thus conserving momentum of the fluid for a greater distance. However, because of some of the initial assumptions that include constant thermal properties, the nanofluid trials essentially behave as a single-phase fluid with higher thermal conductivity for the most part, so the trends are generally identical but have varying values of average heat transfer coefficients.

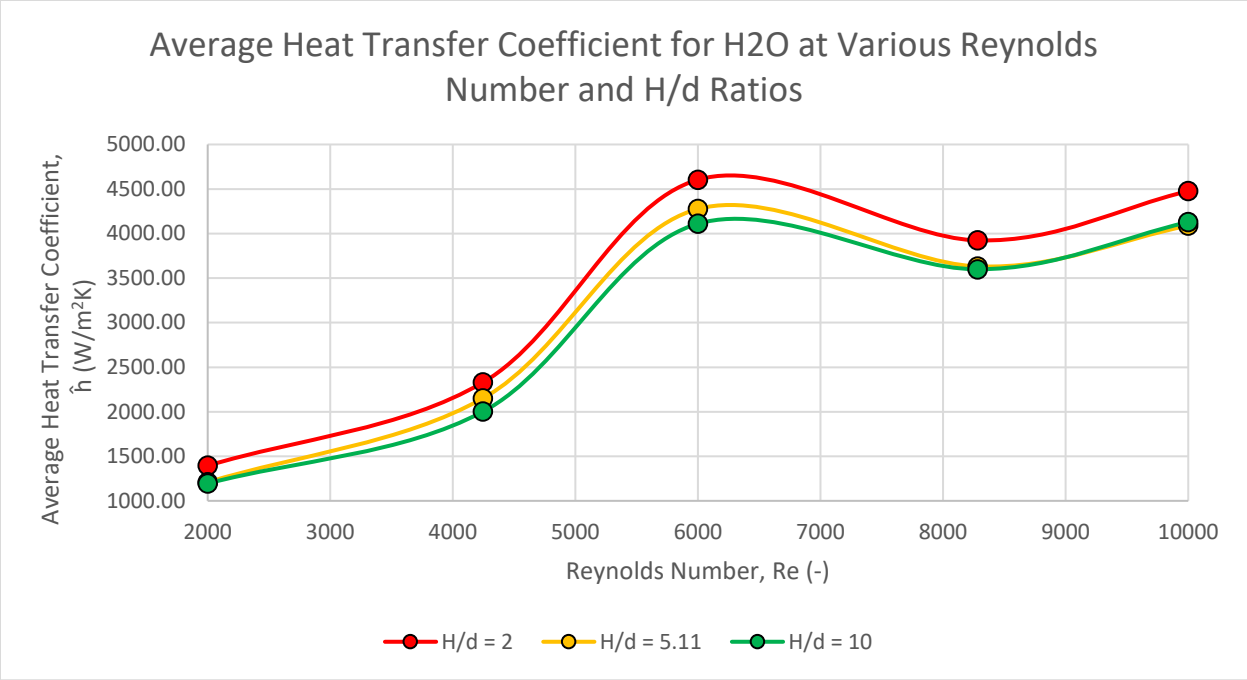

Figure 5.1.1 – Average Heat Transfer Coefficient for H_2O at Various Reynolds Numbers and H/d Ratios

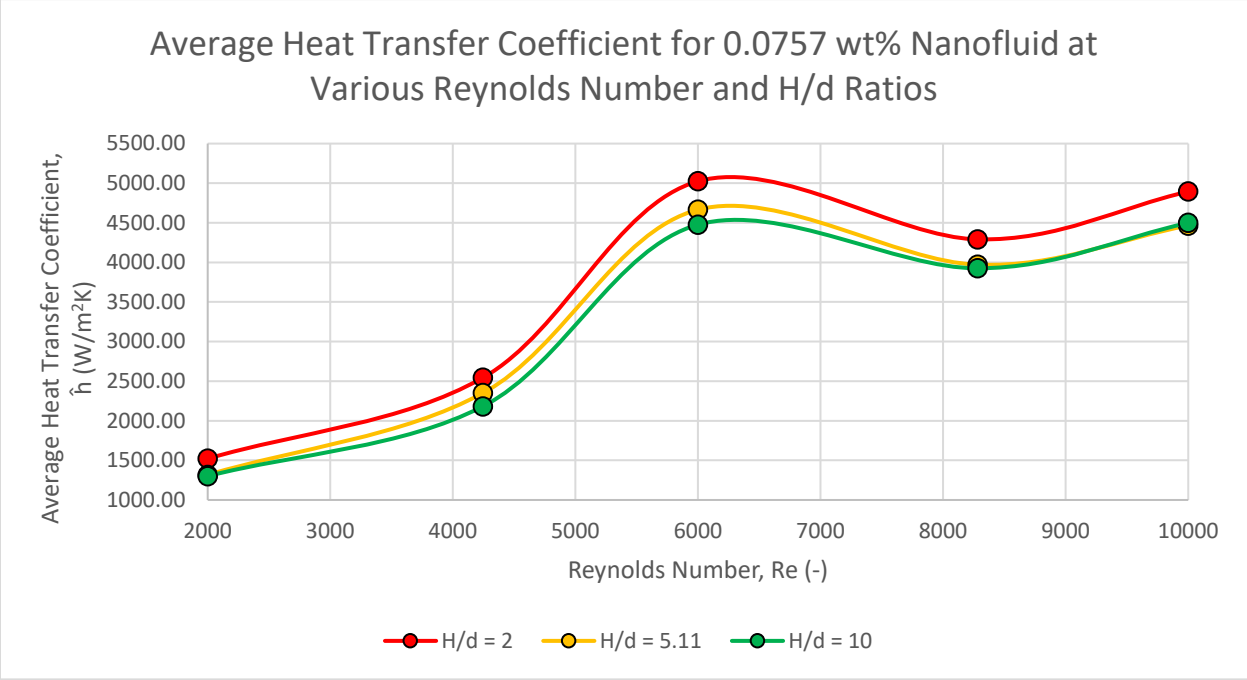

Figure 5.1.2 – Average Heat Transfer Coefficient for 0.0757 wt% Nanofluid at Various Reynolds Numbers and H/d Ratios

5.2 Analysis of the Stagnation Heat Transfer Coefficient for Various Reynolds Numbers and H/d Ratios

In addition to analyzing the average heat transfer coefficient for various Reynolds number and H/d ratios, it is also important to investigate the variation of stagnation heat transfer coefficient for various Reynolds numbers and H/d ratios, which will provide insight into optimizing the overall geometry and parameter selection primarily based on the stagnation region since it provides some of the highest heat transfer coefficients. As shown in Figures 5.2.1 and 5.2.2, it can be ascertained that the three chosen H/d ratios of 2, 5.11, and 10 display consistent patterns similar to the previous section. At low Reynolds numbers (< 6000), the stagnation heat transfer coefficient is maximum when H/d = 2. However, at high Reynolds number (> 7000), the stagnation heat transfer coefficient is maximum when H/d = 10. Again, this relationship is likely due to the lengths of the potential cores in impinging jets, where the length is much larger for large H/d ratios. However, in terms of optimizing the numerical model, a peak stagnation heat transfer coefficient is clearly visible at a Reynolds number of 6000 for an H/d ratio of 2. If using H/d ratios greater than or equal to 10, a Reynolds number of 10000 should be utilized. However, due to the limitations of the scope of the report, other Reynolds numbers and H/d ratios should be tested to confirm the above statements.

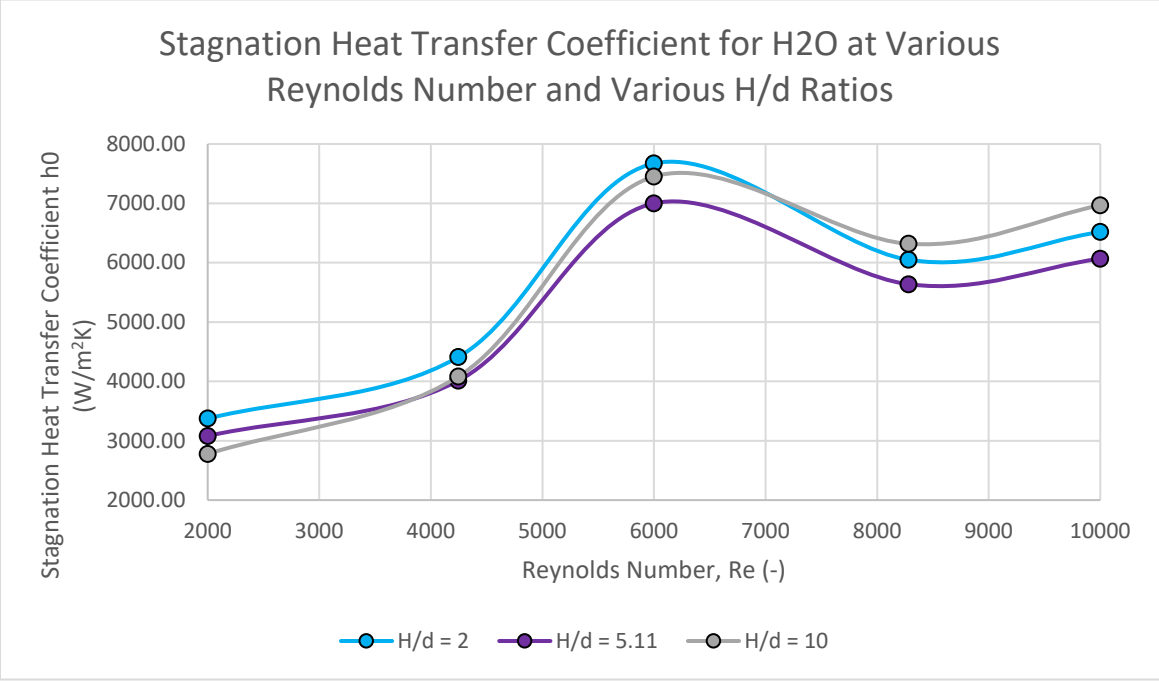

Figure 5.2.1 – H_2O Stagnation Heat Transfer Coefficient

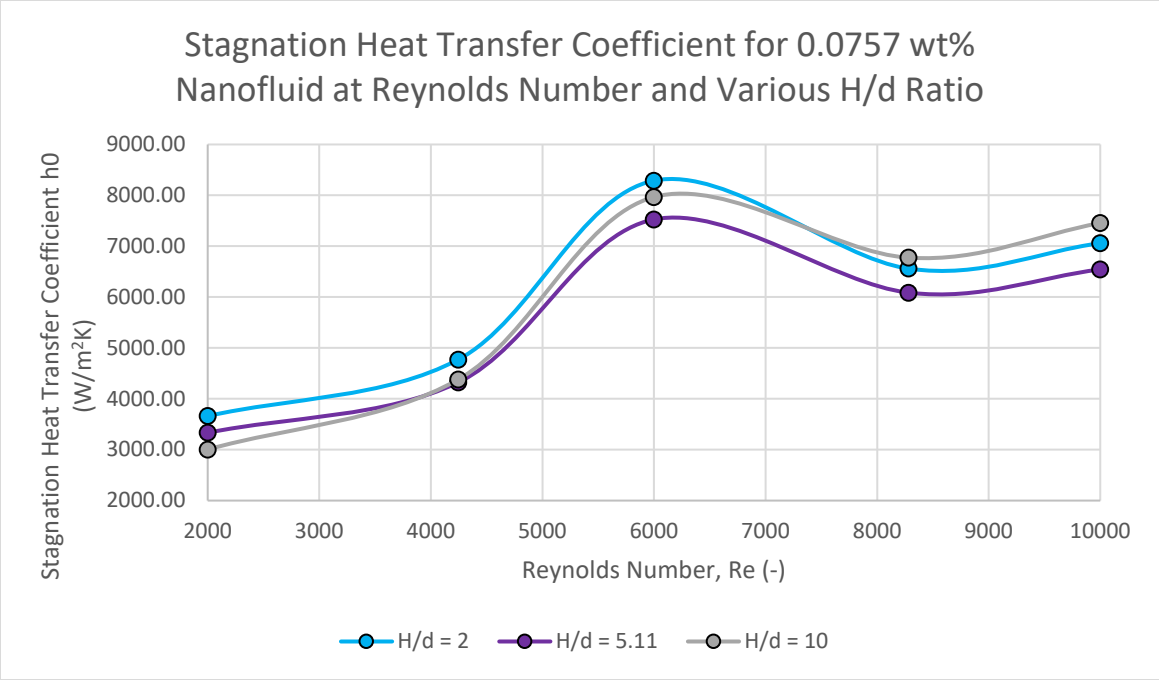

Figure 5.2.2 – 0.0757 wt% Nanofluid Stagnation Heat Transfer Coefficient

5.3 Analysis of the Average Heat Transfer Coefficient for Various Nanofluid Concentration, Reynolds Numbers, and H/d Ratios

In addition, the analysis of the variation of nanofluid concentration (along with base fluid) for various Reynolds numbers and H/d ratios was investigated to determine the effectiveness of nanofluid concentrations shown in Figures 5.3.1 to 5.3.3. Similar to the trends depicted in section 5.1 and 5.2, the average heat transfer coefficient for the base fluid of water and different nanofluid concentrations indicate a peak at a Reynolds number of approximately ~6300. However, the difference between various nanofluid concentrations and water have substantial difference after a Reynolds number of approximately 5500, particularly between the nanofluid concentrations of 0.0353 wt% and 0.0597 wt%.

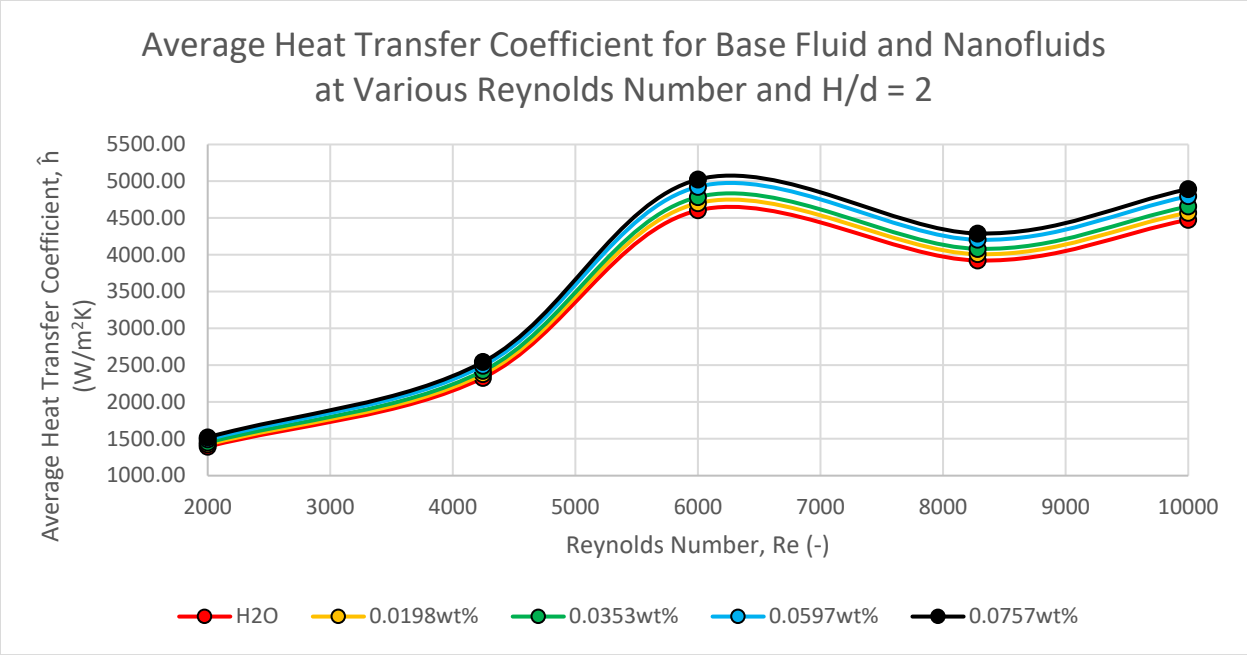

Figure 5.3.1 – Variation of Nanofluid Concentration with Reynolds Number and H/d = 2

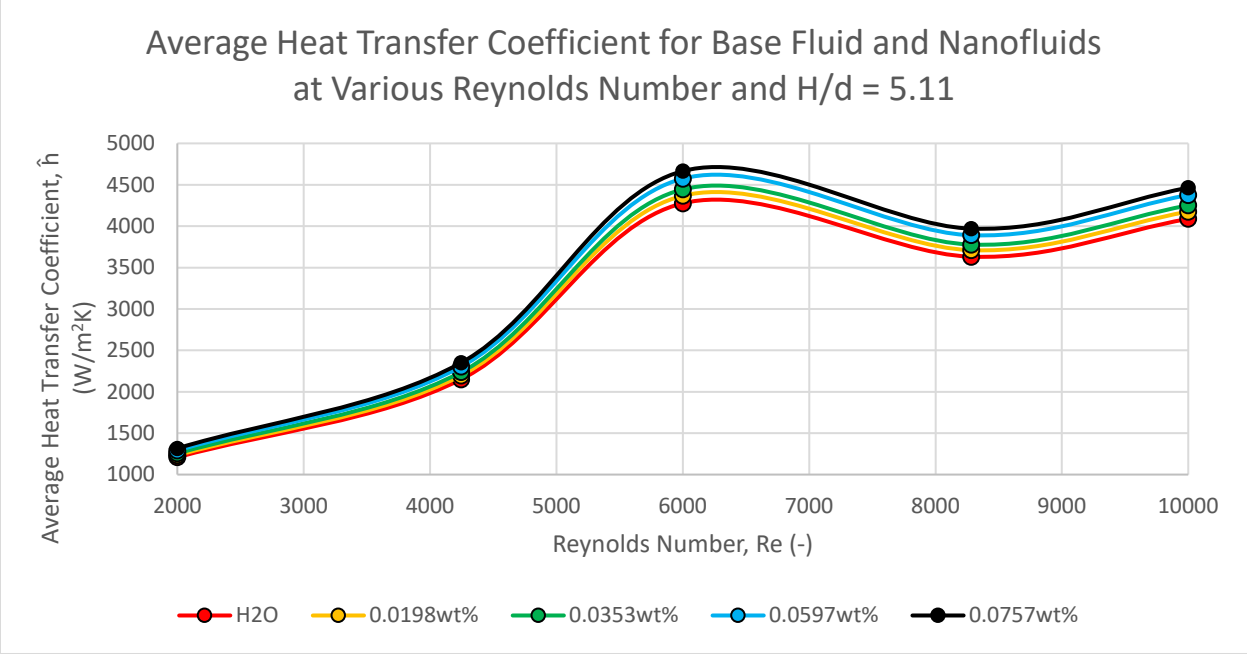

Figure 5.3.2 – Variation of Nanofluid Concentration with Reynolds Number and H/d = 5.11

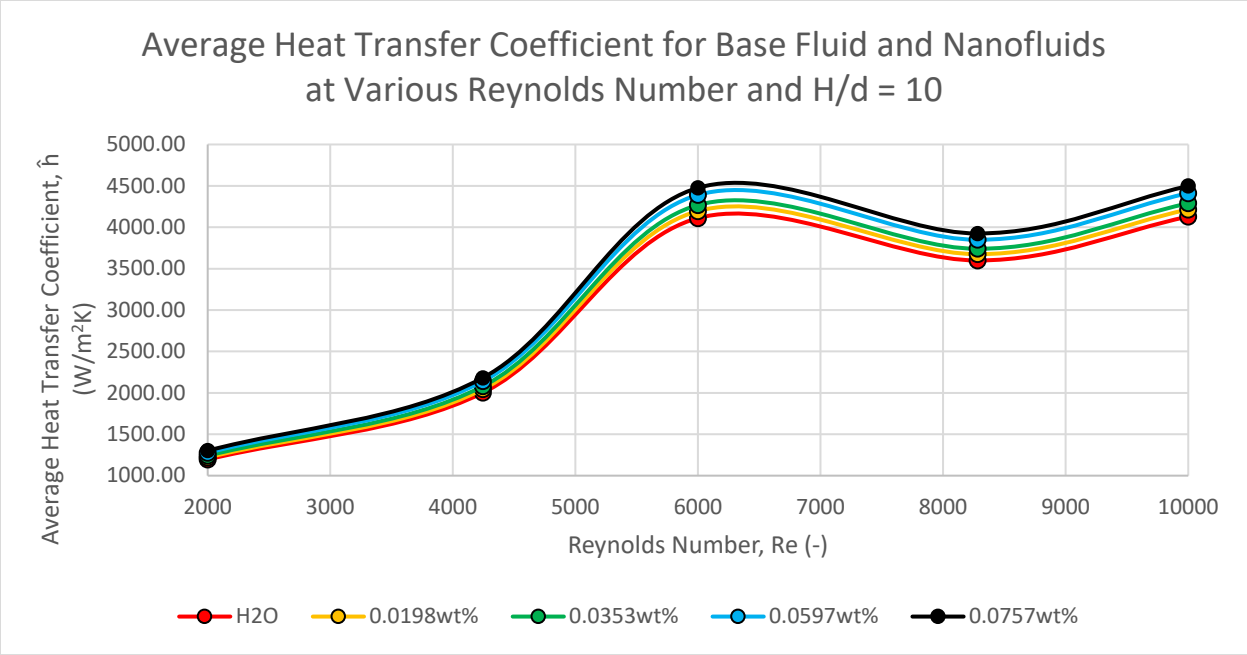

Figure 5.3.3 – Variation of Nanofluid Concentration with Reynolds Number and H/d = 10

5.4 Analysis of the Variation of Local Heat Transfer Coefficient vs. Radial Distance for Various Reynolds Numbers and H/d Ratios

Figures 5.4.1 to 5.4.6 depict the local heat transfer coefficient vs. the radial distance for various Reynolds numbers and H/d ratios mentioned previously. From a general analysis of these figures and data, it can be seen that the overall heat transfer coefficient increases by a significant factor when utilizing a nanofluid concentration up to 0.0757 wt% in comparison to H_2O. Additionally, increasing the Reynolds number results in a relatively proportional increase in the local heat transfer coefficient, especially near the stagnation region of the flow. However, it can be observed that the maximum local heat transfer coefficient occurs for a Reynolds number of 6000, not 10000, which is likely due to the physics and constraints set out in the numerical model.

Following the stagnation region, the wall jet region depicts that an increase in the Reynolds number will proportionally lead to an increase in the local heat transfer coefficient, except for a Reynolds number of 6000 and above, where values, such as 8282, actually results in a slightly lower overall local heat transfer coefficient, while a value of 10000 will have proportionally similar local heat transfer coefficient values or slightly greater than at 6000. This relationship seems to hold true for

H/d ratios up to 10 by a slight margin. It can also be ascertained that greater H/d ratios do not exhibit an explicit second bump, as opposed to smaller H/d ratios, which again holds true for the numerical model.

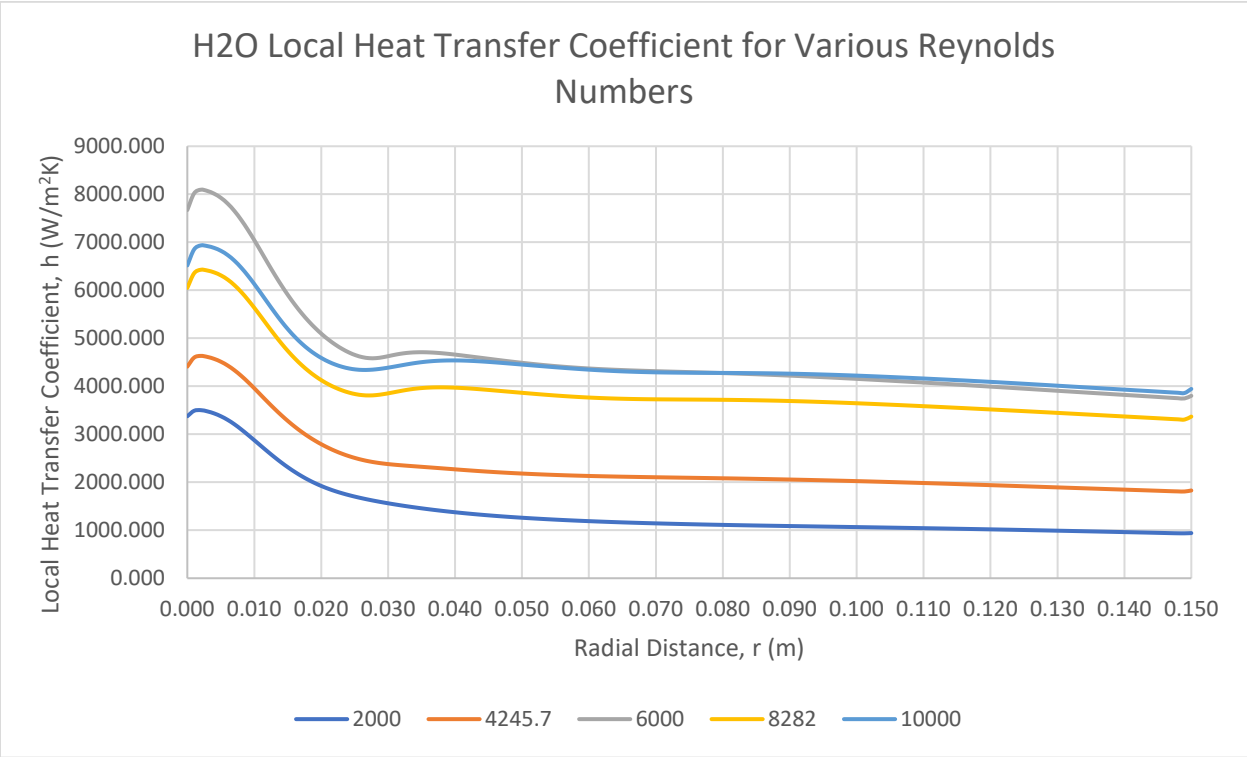

Figure 5.4.1 – Local Heat Transfer Coefficient vs. Radial Distance for H_2O at H/d = 2

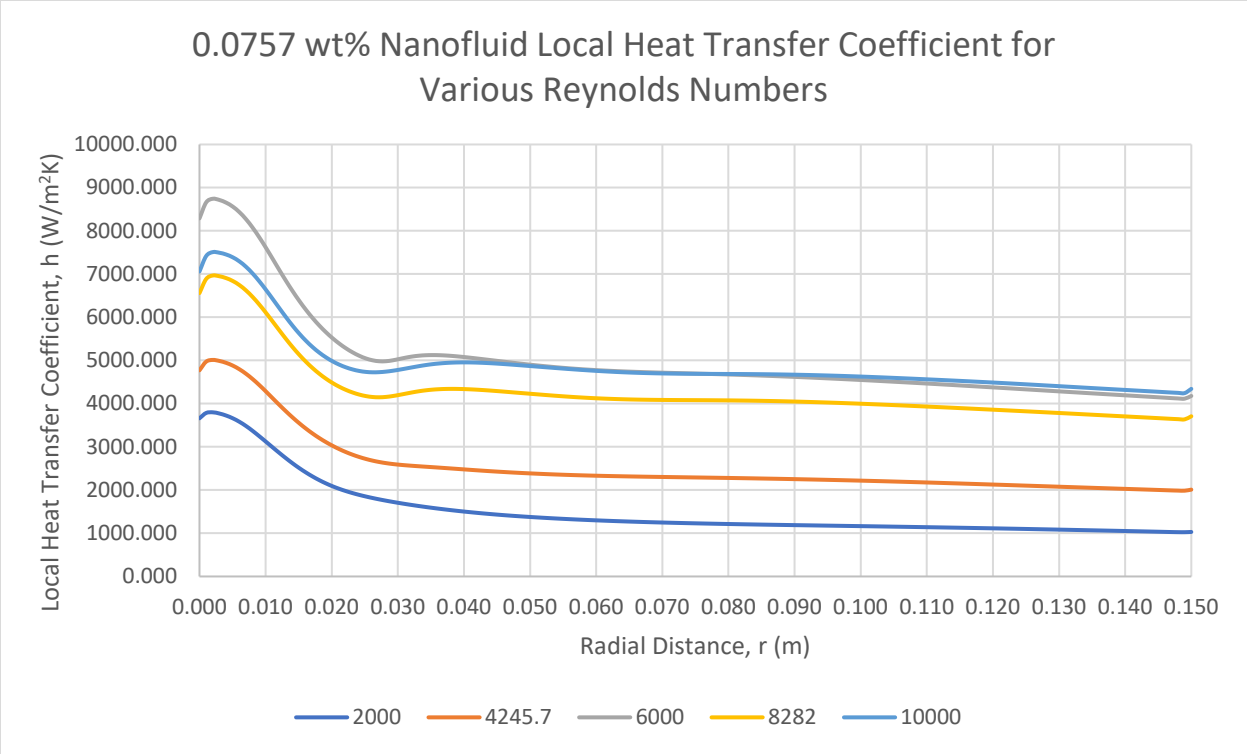

Figure 5.4.2 – Local Heat Transfer Coefficient vs. Radial Distance for 0.0757 wt% at H/d = 2

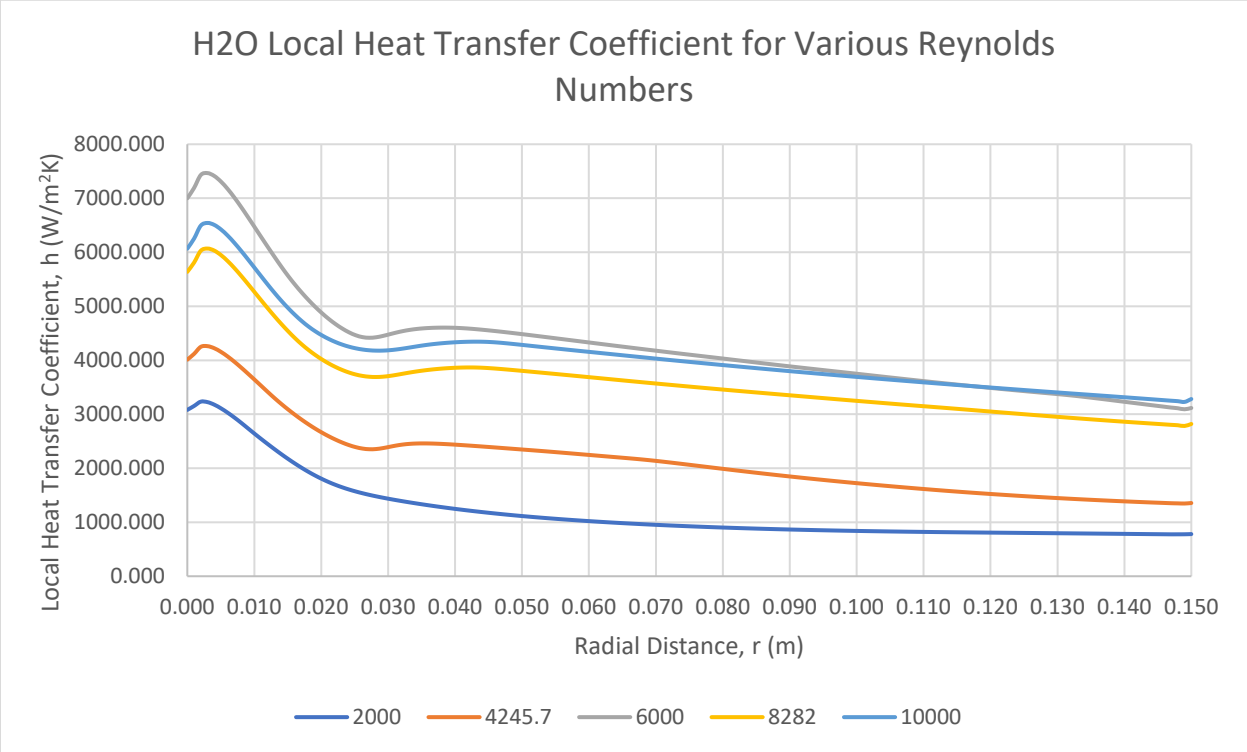

Figure 5.4.3 – Local Heat Transfer Coefficient vs. Radial Distance for H_2O at H/d = 5.11

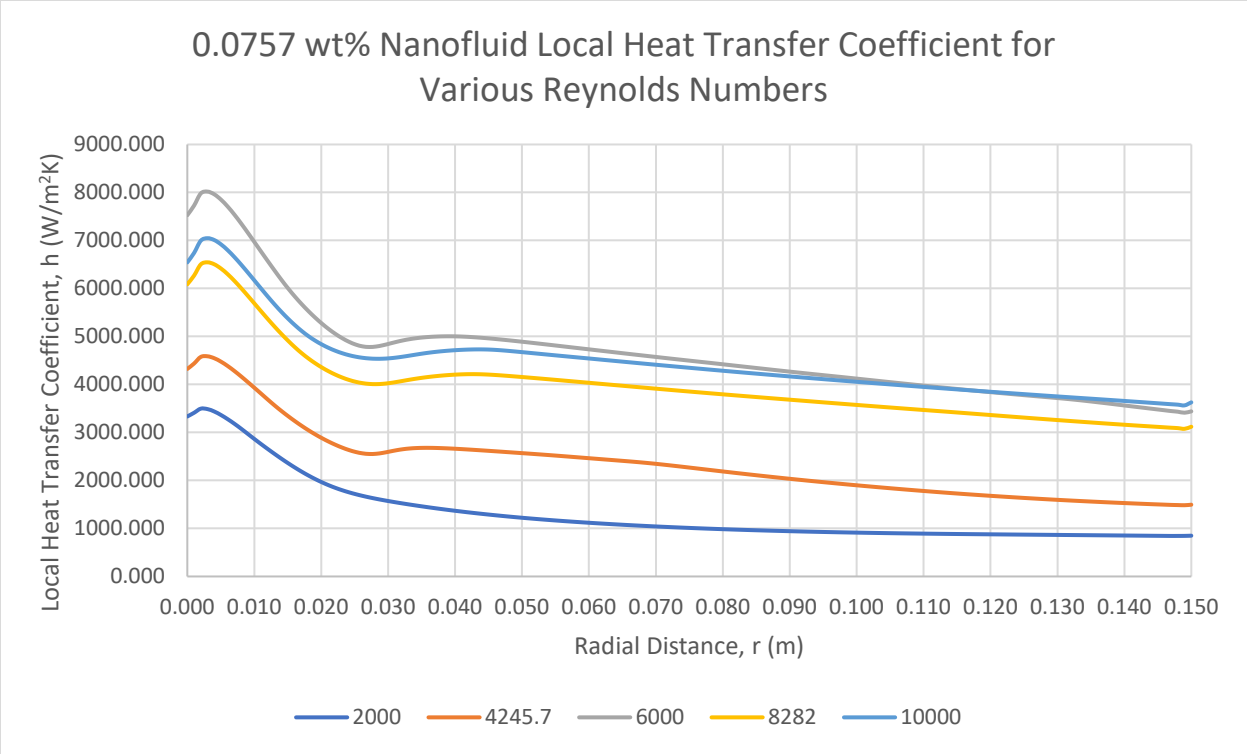

Figure 5.4.4 – Local Heat Transfer Coefficient vs. Radial Distance for 0.0757 wt% at H/d = 5.11

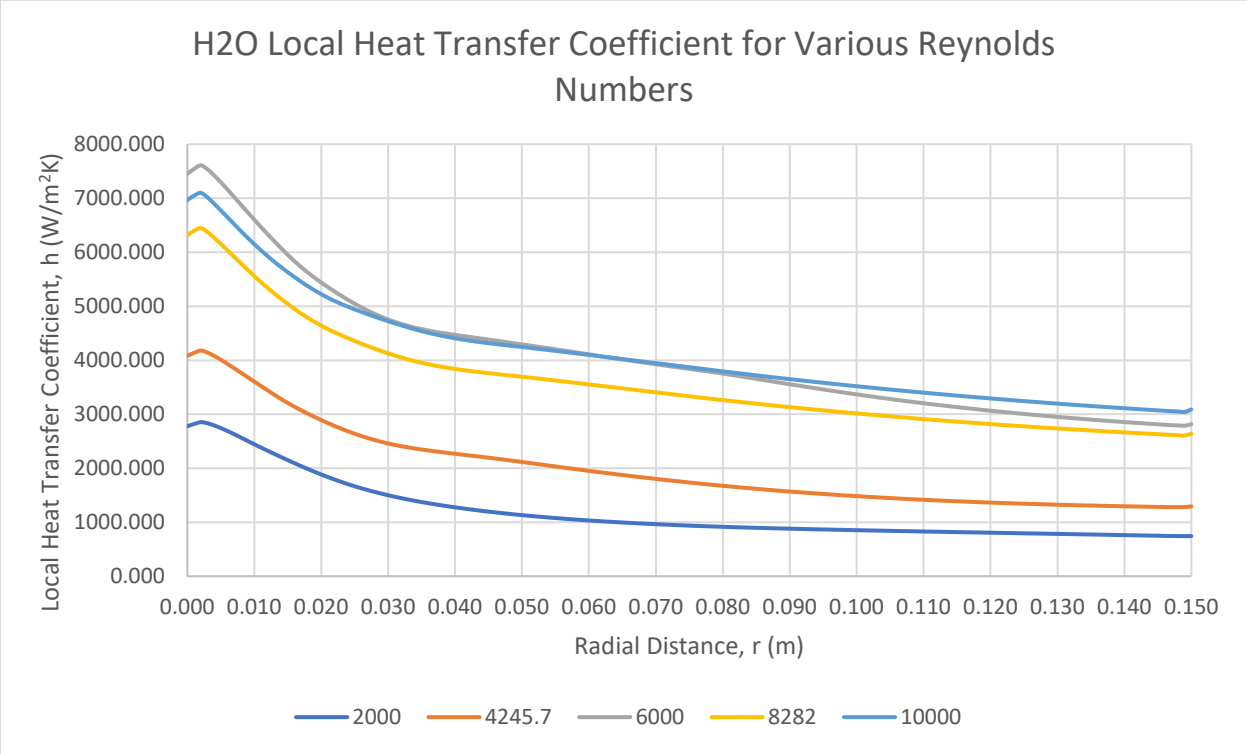

Figure 5.4.5 – Local Heat Transfer Coefficient vs. Radial Distance for H_2O at H/d = 10

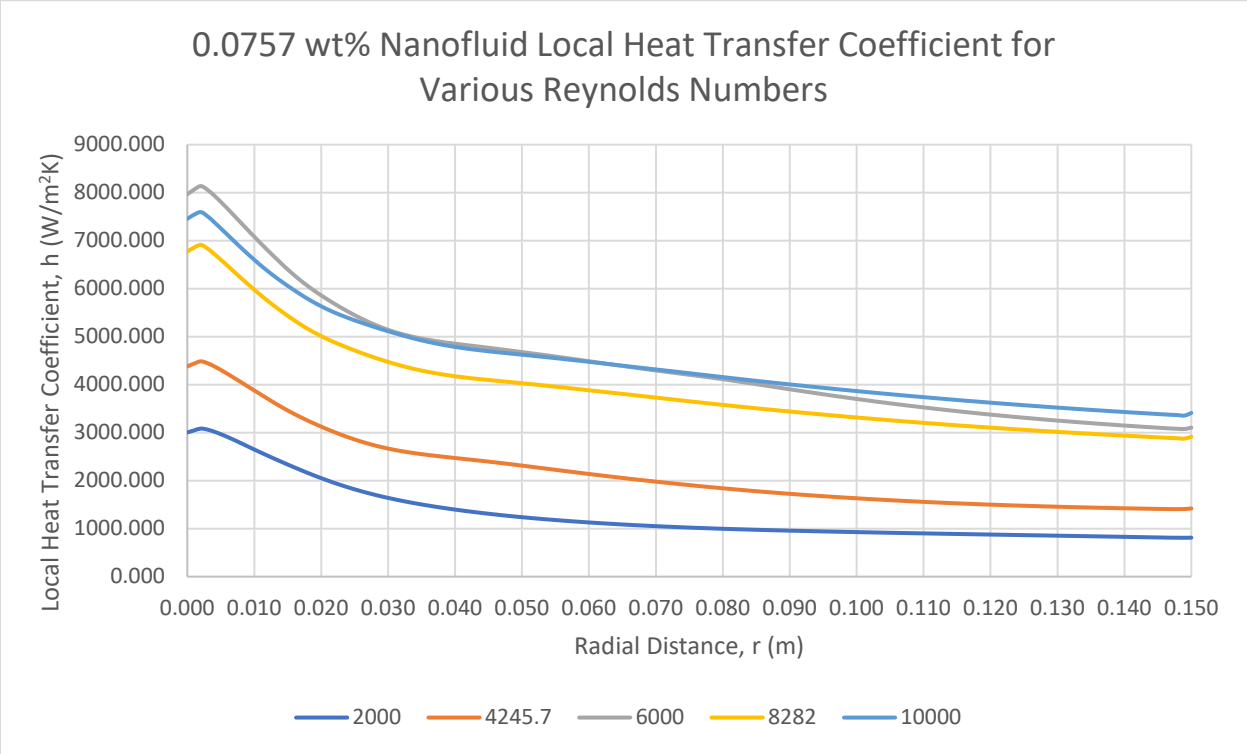

Figure 5.4.6 – Local Heat Transfer Coefficient vs. Radial Distance for 0.0757 wt% at H/d = 10

6.0 Error Analysis

As briefly mentioned in other sections of this report, several errors were discovered when validating the experimental model, which were outlined in sections 4.1 and 4.2. Although two Reynolds number cases of 4245.7 and 8282 were examined, varying degrees of error associated between the experimental and numerical data were present. In summary, percentage errors for Reynolds numbers of 4245.7 and 8282 had averages below 20.802% and 63.878% respectively. However, some of the unusual characteristics regarding these percentage errors stem from the fact that for Re = 4245.7, the percentage error was lowest for H_2O, while for Re = 8282, the percentage error was highest for H_2O, indicating that other factors that influence the model. However, both cases are consistent in terms of having the highest percentage errors for the wall jet region of the impinging jet. Although values were relatively accurate for Re = 4245.7, the values were far from accurate for Re = 8282, with respect to the criteria for accuracy as described by Zuckerman & Lior [3].

However, there are several reasons that these large percentage errors occurred in the numerical model, which include i) initial assumptions made, ii) no ideal turbulence model for impinging jet, iii) single-phase fluid characterization, and iv) nanofluid behavior.

Firstly, some of the initial assumptions made, such as inlet/outlet temperatures of 299.15 K and 297.15 K respectively, could have contributed to the error with the numerical model. Assuming constant fluid properties also has drawbacks, given that fluid temperatures vary depending on temperature, and thus could have also affected the model. However, only averages of the temperatures were given, as opposed to explicit temperature values for different experimental test trials. Additionally, given that thermal conductivity is one of the significant properties that define/influence the overall heat transfer, it is also important to note that it varies with respect to temperature. The initial assumption of constant thermal conductivity could have had a significant impact on the resulting heat transfer experienced in the numerical model. Additionally, this was the primary reason that Nusselt number was not utilized to depict performance, because Nusselt number is the ratio of convective to conductive heat transfer, and is thus dependent on constant

thermal conductivity, which in this scenario varies with temperature and cannot necessarily be used to depict trends.

Secondly, in the process of optimizing the turbulence model, very few provided acceptable error percentages, which limited the applicability of a specific turbulence model to an impinging jet. However, the SST k-ω was reasonably well within error ranges as described by several other scholarly sources.

Thirdly, the numerical model was based on a fundamental assumption that involves utilizing single-phase flow, which essentially describes that "…solid particles and base fluid are assumed to be in thermal and hydrodynamic equilibrium, with no velocity slip between phases" [18]. This highlights that the nanofluid can be approximated as a homogenous fluid that has different properties (increased density, thermal conductivity, etc.) from the base fluid and neglects forces between liquid and solid particles [18]. Only the main conservation equations for continuity and momentum are needed to be solved, which generally reduces any numerical instabilities with modeling solid nanoparticles within a base fluid. This type of assumption changes the overall characteristics of the impinging jet, with its underlying assumptions that the fluid is homogenous with its own effective properties, which depicts that the model is not necessarily able to capture these individual features and ultimately increases the error associated with the numerical model. As such, the single-phase model would not be able to predict the heat transfer accurately due to these limitations. In realistic/experimental setups, the fluid is a multiphase model, which has coupling properties between the solid nanoparticles and the base fluid, which have separate properties and characteristics. This analysis goes back to the preparation of nanofluids, given that similar settings can produce widely varying nanofluid properties and that there is no specific baseline for comparison. Multiphase models should be investigated as a means to increase the accuracy of the numerical model.

Lastly, and more importantly, nanofluid behavior is complex to reproduce in a numerical simulation. Brownian motion, varying nanoparticle sizes, non-uniform thermal properties, nanofluid preparation, and several other factors increase the error associated with numerical simulation.

7.0 Future Work

Several aspects of future work and parameters will need to be investigated to produce an accurate model with respect to simulating the behavior of specific nanofluids, which include:

1. Obtaining specific correlations of nanofluid and base fluid properties instead of assuming constant properties,
2. Enhancing the boundary layer resolution to include the optimal amount of boundary layers needed to resolve to model completely without additional layers that would otherwise influence results,
3. Utilizing other numerical simulation software to validate results, and
4. Incorporating other factors that can be assumed to influence experimental results in numerical simulations.

These branches of future work are based on the fact that numerical simulations often have ideal conditions that do not take into account certain realistic parameters, such as nanoparticle dispersion within a base fluid that cannot be readily replicated from experiment to experiment, which is often one of the limits of modeling described in a previous section.

8.0 Review and Conclusions

In conclusion, a review of this report indicates that the behavior of an impinging jet has several complex characteristics. Numerous adjustments can be made to improve the accuracy of the numerical model but are still limited by some of the phenomena associated with nanofluids and their behavior, such as Brownian motion. This report provides a summary of the research and analysis of various experimental and numerical methods completed to provide a thorough and detailed analysis of jet impingement. A numerical model was developed and compared to an experimental model by B. Jaberi et al. [2], with initial assumptions and parameters made accordingly with the availability of information. Turbulence model optimization was conducted to investigate the model that provided the lowest error percentages in comparison to the experimental data, which was determined to be the SST k-ω turbulence model. Further analysis was also conducted to improve on the current model and provide insightful observations when considering testing other Reynolds numbers or H/d ratios for future experimental analysis. Lastly, an analysis for potential errors associated with the numerical model was completed for future consideration of modeling an impinging jet of nanofluid. Overall, an analysis of the numerical results for determining the heat transfer coefficient with respect to the radial distance shows relatively good trends with experimental data, with the exception of some abnormal errors due to a number of reasons outlined in section 6.0.

References

1. Chaudhari, M., Puranik, B., & Agrawal, A. (2010). Heat transfer characteristics of synthetic jet impingement cooling. *International Journal of Heat and Mass Transfer*, *53*, 1057-1069. doi:10.1016/j.ijheatmasstransfer.2009.11.005
2. Jaberi, B., Yousefi, T., Farahbakhsh, B., & Saghir, M. (2013). Experimental investigation on heat transfer enhancement due to Al2O3–water nanofluid using impingement of round jet on circular disk. *International Journal of Thermal Sciences*, *74*, 199-207. doi:10.1016/j.ijthermalsci.2013.06.013
3. Zuckerman, N., & Lior, N. (2006). Jet Impingement Heat Transfer: Physics, Correlations, and Numerical Modeling. *Advances in Heat Transfer*, *39*, 565-631. doi:10.1016/s0065-2717(06)39006-5
4. Cho, H. H., Kim, K. M., & Song, J. (2011). Applications of Impingement Jet Cooling Systems. *Cooling Systems: Energy, Engineering and Applications*, 37-67.
5. Anwarullah, M., Vasudeva Rao, V., & Sharma, K. V. (2012). Experimental investigation for enhancement of heat transfer from cooling of electronic components by circular air jet impingement. *Heat and Mass Transfer*, *48*(9), 1627-1635. doi:10.1007/s00231-012-1005-y
6. Jayaraman, S. (2013). Micro Scale Jet Impingement Cooling and its Efficacy on Turbine Vanes: A Numerical Study. Aerospace Engineering - Ryerson University, 1-60.
7. O'Donovan, T. S. (2005). Fluid Flow and Heat Transfer of an Impinging Air Jet.
8. Jensen, M. V., & Walther, J. H. (2013). Numerical Analysis of Jet Impingement Heat Transfer at High Jet Reynolds Number and Large Temperature Difference. *Heat Transfer Engineering*, *34*(10), 801-809. doi:10.1080/01457632.2012.746153
9. Mills, A. F., & Ganesan, V. (1999). *Heat Transfer* (2nd ed.). Pearson Education.
10. Livingood, J. B., & Hrycak, P. (1973). Impingement Heat Transfer from Turbulent Air Jets to Flat Plates - A Literature Survey. National Aeronautics and Space Administration, 1-42.
11. Wu, J., & Zhao, J. (2013). A review of nanofluid heat transfer and critical heat flux enhancement—Research gap to engineering application. *Progress in Nuclear Energy*, *66*, 13-24. doi:10.1016/j.pnucene.2013.03.009

12. Wang, X., & Mujumdar, A. S. (2006). Heat transfer characteristics of nanofluids: a review. *International Journal of Thermal Sciences*, *46*, 1-19. doi:10.1016/j.ijthermalsci.2006.06.010
13. Wen, D., Lin, G., Vafaei, S., & Zhang, K. (2009). Review of nanofluids for heat transfer applications. *Particuology*, *7*(2), 141-150. doi:10.1016/j.partic.2009.01.007
14. Zeitoun, O., Ali, M., & Al-Ansary, H. (2013). The Effect of Particle Concentration on Cooling of a Circular Horizontal Surface using Nanofluid Jets. *Nanoscale and Microscale Thermophysical Engineering*, *17*, 154-171. doi:10.1080/15567265.2012.749963
15. Sharma, K. V., Sarm, P. K., Azmi, W. H., Mamat, R., & Kadirgama, K. (2012). Correlations to Predict Friction and Forced Convection Heat Transfer Coefficients of Water Based Nanofluids for Turbulent Flow in a Tube. *International Journal of Microscale and Nanoscale Thermal and Fluid Transfer Phenomena*, *3*(4), 283-307.
16. El Bécaye Maïga, S., Nguyen, C. T., Galanis, N., Roy, G., Maré, T., & Coqueux, M. (2006). Heat transfer enhancement in turbulent tube flow using Al2O3 nanoparticle suspension. *International Journal of Numerical Methods for Heat & Fluid Flow*, *16*(3), 275-292. doi:10.1108/09615530610649717
17. White, F. M. (2003). *Fluid Mechanics* (5th ed.). McGraw-Hill.
18. Peng, W., Jizu, L., Minli, B., Yuyan, W., & Chengzhi, H. (2014). A Numerical Investigation of Impinging Jet Cooling with Nanofluids. *Nanoscale and Microscale Thermophysical Engineering*, *18*(4), 329-353. doi:10.1080/15567265.2014.921749